RSC Advances

ROYAL SOCIETY OF CHEMISTRY

PAPER

View Article Online
View Journal | View Issue

Cite this: *RSC Adv.*, 2024, **14**, 5675

Intrinsic dynamic and static natures of $^{A}Pn–X^{+}–^{B}Pn$ σ(3c–4e) type interactions ($^{A}Pn = ^{B}Pn$ = N, P, As and Sb; X = H, F, Cl, Br and I) in bicyclo[3.3.3] and bicyclo[4.4.4] systems and their behaviour, elucidated with QTAIM dual functional analysis†

Taro Nishide, Waro Nakanishi and Satoko Hayashi *

Received 29th December 2023
Accepted 9th January 2024

DOI: 10.1039/d3ra08926f

rsc.li/rsc-advances

The intrinsic dynamic and static natures of $^{A}Pn–X^{+}–^{B}Pn$ ($^{A}Pn = ^{B}Pn$: N, P, As and Sb; X = H, F, Cl, Br and I) in **1a**$^{+}$–**8c**$^{+}$ were elucidated with the quantum theory of atoms-in-molecules dual functional analysis (QTAIM-DFA). Species **1a**$^{+}$–**8c**$^{+}$ were formed by incorporating X^{+} between ^{A}Pn and ^{B}Pn of $^{A}Pn(CH_2CH_2CH_2)_3{}^{B}Pn$ (**1**–**4**) and $^{A}Pn(CH_2CH_2CH_2CH_2)_3{}^{B}Pn$ (**5**–**8**). The relative stabilities between the symmetric and nonsymmetric structures along with their transition states were investigated. Various natures from typical hydrogen bonds (t-HB) to classical covalent bonds were predicted for the $^{A}Pn–X/^{B}Pn–X$ interactions in $^{A}Pn–X^{+}–^{B}Pn$ with QTAIM-DFA. The secondary interactions of H–H and X–C were also detected. The vdW to molecular complexes through charge transfer natures were predicted for them. Natural bond orbital analysis clarified that the CT terms were caused by not only $n(^{A}Pn) \rightarrow \sigma^{*}(X–^{B}Pn)$ but also $\sigma(^{A}Pn–C) \rightarrow \sigma^{*}(X–^{B}Pn)$, $\sigma(^{A}Pn–C/^{B}Pn–C) \rightarrow n_p(X^{+})$ and $n(X) \rightarrow n_s(Pn^{+})$. The direction and magnitude of the p-character of $n(^{A}Pn)$ were the factors that determined the types of donor–acceptor interactions. Estimating the order of the interaction strengths was attempted. The σ(3c–4e) characters of $^{A}Pn–X^{+}–^{B}Pn$ were also examined by analysing the charge distributions on $^{A}Pn–X^{+}–^{B}Pn$. These results would provide fundamentally important insight into designing molecules with high functionality containing X^{+} in symmetric and nonsymmetric structures.

Introduction

Chemical bonds and interactions are the most important concepts in chemical and biological sciences. Intrinsic dynamic and static natures of various types of chemical bonds and interactions have been elucidated with the quantum theory of atoms-in-molecules dual functional analysis (QTAIM-DFA).[1–4] Hydrogen bonds[5] and chalcogen bonds[6] are the typical examples of such interactions. What are the natures of the non-covalent interactions, that play a highly important role in the biological systems, such as enzymes? The next target of our project is to elucidate the natures of such interactions, that play a highly important role in the biological species, by applying QTAIM-DFA. It is well known that conformations of the reaction sites, in highly efficient enzymatic reactions, for example, are highly controlled. It is necessary to accumulate fundamental knowledge on the behavior of such interactions under the conditions, to achieve the above goal. The natures of the interactions in cage compounds, called atranes, are investigated, as a first stage of our investigations.

Many cage compounds have been prepared, so far, and they play an important role in chemistry.[7,8] Bicyclo[3.3.3]undecane (**I**) and bicyclo[4.4.4]tetradecane (**II**) provide typical types of the frameworks. The bridgehead carbon distances in **I** and **II** are considered to be the medium size. The original interactions between the methine groups in **I** and **II** would be negligibly small. However, if the methine groups are replaced by A and A′ of the main group atoms or the derivatives in the neutral and charged forms, the A⋯A′ interactions become much stronger. The A⋯A′ interactions make it possible to investigate the natures of the interactions in more detail. The interactions would consist of the repulsive and/or attractive terms. The A⋯A′ interactions change greatly the energy profiles around the interactions relative to the original cases. The changes have profound effects not only on the fine details of the structures but also on the natures of the interactions, which are to be elucidated.

Among a lot of such species,[9–13] the research group of Kawashima demonstrated that 1-hydro-5-carbaphosphatrane and 1-hydro-6-carbaphosphatrane could form an "anti-

---

Faculty of Systems Engineering, Wakayama University, 930 Sakaedani, Wakayama 640-8510, Japan. E-mail: hayashi3@wakayama-u.ac.jp

† Electronic supplementary information (ESI) available: Additional tables and figures, explanation of QTAIM-DFA, and the fully optimized and transition structures given by Cartesian coordinates, together with total energies of **1a**$^{+}$–**8c**$^{+}$. See DOI: https://doi.org/10.1039/d3ra08926f

apicophilic" arrangement.[14–17] Thus, the skeletons of **I** and **II** could supply the diverse electronic structures and have unique functionalities, such as superbase,[18–20] catalysis[21–23] and biological activity.[24–27] Alder and coworkers synthesized various derivatives of **I** and **II** and related species.[9,11,28–31] 1,5-Diazabicyclo[3.3.3]undecane (**1**)[28] and 1,6-diazabicyclo[4.4.4]tetradecane (**5**)[29] are the typical examples. They reported protonation in cages of various sizes.[32–36] Much attention has been paid to prepare the species with the interactions of the so-called proton sponges and to clarify the properties. While **5** could contain a proton in the cage to form a $[\mathrm{N–H–N}]^+$ bond, N is protonated from outside the cage in **1**. However, Alder mentioned that **1** containing a proton in the cage could potentially be kinetically persistent if once formed.[34]

Recently, molecular designs to form $[\mathrm{N}\cdots\mathrm{F–N}]^+$ were theoretically proposed by using the skeletons of **1** and **5**,[37] in addition to $[\mathrm{C–H–C}]^-$ using the bicyclo[3.3.3]undecane backborn.[38,39] Much effort has been made experimentally and theoretically to clarify properties of the symmetric (sym) and nonsymmetric (nsym) interactions of the $[\mathrm{N–X–N}]^+$ (X = F, Cl, Br and I) form.[40–44] However, few reports seem to contain the systematic research on the compressed $[\mathrm{N–X–N}]^+$ interactions (X = F, Cl, Br and I) in cage structures of the medium size.

Our investigations were focused to elucidate the natures and the properties of the interactions in $[\mathrm{N–X–N}]^+$ (X = H, F, Cl, Br and I) and the pnictogen derivatives, to achieve our purpose. Chart 1 shows the structures of **1a**$^+$–**8e**$^+$ and the definition of the symmetric (sym) and nonsymmetric (nsym) shapes. The $[^{\mathrm{A}}\mathrm{Pn–X–}^{\mathrm{B}}\mathrm{Pn}]^+$ interaction will form through the incorporation of X$^+$ into $^{\mathrm{A}}\mathrm{Pn}\cdots{}^{\mathrm{B}}\mathrm{Pn}$ of **1–8**. Herein, we report the results of the investigations on $[^{\mathrm{A}}\mathrm{Pn–X–}^{\mathrm{B}}\mathrm{Pn}]^+$ in **1a**$^+$–**8e**$^+$, using the original frameworks of **I** and **II**, where $^{\mathrm{A}}$Pn = $^{\mathrm{B}}$Pn = N (**1*x***$^+$/**5*x***$^+$), P (**2*x***$^+$/**6*x***$^+$), As (**3*x***$^+$/**7*x***$^+$) and Sb (**4*x***$^+$/**8*x***$^+$); X = H (***x*** = **a**), F (**b**), Cl (**c**), Br (**d**) and I (**e**) (see Chart 1). The nature of $[^{\mathrm{A}}\mathrm{Pn–X–}^{\mathrm{B}}\mathrm{Pn}]^+$ in **1a**$^+$–**8e**$^+$ was elucidated after clarifying the structural features and energetic behaviour of the species. The subscribe $^+$ as in $[^{\mathrm{A}}\mathrm{Pn–X–}^{\mathrm{B}}\mathrm{Pn}]^+$ will be often omitted from the interaction as in $^{\mathrm{A}}\mathrm{Pn–X–}^{\mathrm{B}}\mathrm{Pn}$, in this paper. It is the second issue of this study to clarify the stabilities and the properties of **1–8** and **1a**$^+$–**8e**$^+$ with the larger pnictogen atoms, in place of the CH groups, at the bridgehead positions of **I** and **II**. The results of this study will provide useful insight into the $^{\mathrm{A}}\mathrm{Pn–X–}^{\mathrm{B}}\mathrm{Pn}$ σ(3c–4e) interactions such as those in **1a**$^+$–**8e**$^+$.

Survey of quantum theory of atoms-in-molecules dual functional analysis (QTAIM-DFA)

The natures of the $^{\mathrm{A}}\mathrm{Pn–X–}^{\mathrm{B}}\mathrm{Pn}$ σ(3c–4e) type interactions are calculated with QTAIM-DFA,[1–4] which we proposed. QTAIM-DFA is formulated based on the QTAIM approach, introduced by Bader.[45,46] QTAIM-DFA has elucidated the (intrinsic) dynamic and static natures of various interactions. The bond critical point (BCP, *) is an important concept in the QTAIM approach.[45,46] The charge density ($\rho(\boldsymbol{r})$) at the BCP is described by $\rho_{\mathrm{b}}(\boldsymbol{r}_{\mathrm{c}})$, as are other QTAIM functions, such as the total electron energy densities $H_{\mathrm{b}}(\boldsymbol{r}_{\mathrm{c}})$, potential energy densities $V_{\mathrm{b}}(\boldsymbol{r}_{\mathrm{c}})$ and kinetic energy densities $G_{\mathrm{b}}(\boldsymbol{r}_{\mathrm{c}})$ at BCPs. A chemical bond or interaction between atoms A and B is denoted by A–B, which corresponds to the bond path (BP) in QTAIM. We will use A-*-B for the BP, in which the asterisk emphasizes the existence of a BCP in A–B. In a nonsymmetric shape, the interaction between $^{\mathrm{A}}$Pn and X is defined to be longer than for $^{\mathrm{B}}$Pn and X, therefore, they are often described as $^{\mathrm{A}}$Pn–*–X and $^{\mathrm{B}}$Pn-*-X, respectively, which means $^{\mathrm{A}}\mathrm{Pn}\cdots\mathrm{X}$ and $^{\mathrm{B}}$Pn–X, respectively. The long distances between A and B also denoted by A$\cdots$B, irrespective of above definition.

In the QTAIM approach, $H_{\mathrm{b}}(\boldsymbol{r}_{\mathrm{c}})$ is plotted *versus* $H_{\mathrm{b}}(\boldsymbol{r}_{\mathrm{c}}) - V_{\mathrm{b}}(\boldsymbol{r}_{\mathrm{c}})/2$ at the BCPs on the interactions in question. The plots are called QTAIM-DFA plots.[1,2] Data from the perturbed structures around the fully optimized structures are plotted in QTAIM-DFA, in addition to the data from the fully optimized ones, in our treatment. Each plot for an interaction is analysed by the polar coordinate (R, θ) parameters with the (θ_{p}, κ_{p}) ones. The R and θ parameters are calculated for the data point of the interaction in the fully optimized structure at the origin. While R corresponds to the energy for the interaction in question in the plot, θ, measured from the y-axis, classifies the interaction. The (θ_{p}, κ_{p}) parameters are measured based on the plot at the data point for the interaction in the fully optimized structure. θ_{p} is measured from the y-direction, which corresponds to the tangent line of the plot, and κ_{p} is the curvature.[1] While θ_{p} characterizes the interaction, κ_{p} does not play an important role in the analysis, although it may contain deep meaning.

The (R, θ) parameters are calculated based on the data from the fully optimized structures; therefore, they correspond to the static nature of interactions. The dynamic nature of interactions is proposed based on (θ_{p}, κ_{p}), which are obtained by analysing the plots. The plots contain the data from the fully optimized and perturbed structures around fully optimized ones. The perturbed structures are generated using the coordinates ($\boldsymbol{C}_i$) derived from the diagonal elements of the compliance constants (C_{ii}) for the internal vibrations, in CIV.[47] The values were calculated using Compliance 3.0.2 program.[48,49] The dynamic nature based on the perturbed structures with CIV is described as the "intrinsic dynamic nature" since the coordinates are invariant to the choice of coordinate system and thus the perturbed structures are highly reliable.[47] The standard criteria that distinguish the interactions in question from others are obtained by applying QTAIM-DFA to standard interactions.[1–4] The criteria and QTAIM-DFA with the basic concept of the QTAIM approach are shown by Scheme SA1–SA3, Fig. SA1, SA2, Table SA1 and eqn (SA1)–(SA7) of the ESI.†

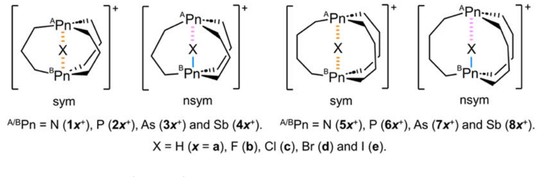

Chart 1 Species **1a**$^+$–**8e**$^+$ and the definition of the symmetric (sym) and nonsymmetric (nsym) shapes.

Methodological details in calculations

Gaussian 09 program was used for the calculations.[50] Various basis set systems (BSSs) were examined to determine suitable

BSSs. Table 1 shows typical BSSs, examined. The BSS-A employs the basis sets of the Sapporo-TZP with diffuse functions of the 1s1p type (Sapporo-TZP + 1s1p) for all atoms, as implemented from the Sapporo Basis Set Factory.[51] BSS-B employs Sapporo-TZP + 1s1p for ^{A}Pn, ^{B}Pn and (X = H, F, Cl, Br and I), together with Sapporo-DZP + 1s1p for C and H. For BSS-C, Sapporo-TZP + 1s1p is applied to ^{A}Pn, ^{B}Pn and X, whereas Sapporo-DZP is applied to C and H. The Møller–Plesset second order energy correlation (MP2) level[52] was employed for the calculations (MP2/BSS-A, MP2/BSS-B and MP2/BSS-C). The optimized structures were confirmed by frequency analysis. The results of frequency analysis were used to derive the coordinates $\boldsymbol{C}_i$ and the constants C_{ii}. Natural bond orbital (NBO) analysis was performed by the NBO6 program[53] under M06-2X/BSS-B//MP2/BSS-B. The relativistic effects were not considered, which would be the next them of the study, especially on the element of 5th period of Sb and I.

Eqn (1) explains the process to generate the perturbed structures with CIV.[47] The kth perturbed structure in question ($\boldsymbol{S}_{\mathrm{kw}}$) was generated by adding the coordinates of $\boldsymbol{C}_i$ to the standard orientation of a fully optimized structure ($\boldsymbol{S}_{\mathrm{o}}$) in the matrix representation. The coefficient g_{kw} controls the structural difference between $\boldsymbol{S}_{\mathrm{kw}}$ and $\boldsymbol{S}_{\mathrm{o}}$. g_{kw} was determined to satisfy r in eqn (2), where r and r_{o} are the interaction distances in question in perturbed structures and a fully optimized structure, respectively, and a_{o} is the Bohr radius (0.52918 Å). The $\boldsymbol{C}_i$ values of six digits were used to calculate the $\boldsymbol{S}_{\mathrm{kw}}$.

$$\boldsymbol{S}_{\mathrm{kw}} = \boldsymbol{S}_{\mathrm{o}} + g_{\mathrm{kw}} \cdot \boldsymbol{C}_i \tag{1}$$

$$r = r_{\mathrm{o}} + wa_{\mathrm{o}}\ (w = (0),\ \pm 0.05 \text{ and } \pm 0.1;\ a_{\mathrm{o}} = 0.52918\ \text{Å}) \tag{2}$$

$$y = c_{\mathrm{o}} + c_1x + c_2x^2 + c_3x^3$$
$$(R_{\mathrm{c}}^2 = \text{square of correlation coefficient}) \tag{3}$$

QTAIM functions were analysed by the AIM2000[54] and AIMAll[55] programs. Data from five points of $w = 0$, ± 0.05 and ± 0.1 in eqn (2) were used in a QTAIM-DFA plot, unless otherwise noted. Each plot was analysed by using the regression curve of the cubic function, shown in eqn (3), where $(x, y) = (H_{\mathrm{b}}(\boldsymbol{r}_{\mathrm{c}}) - V_{\mathrm{b}}(\boldsymbol{r}_{\mathrm{c}})/2,\ H_{\mathrm{b}}(\boldsymbol{r}_{\mathrm{c}}))$, with an R_{c}^2 generally greater than 0.99999.[4]

Results and discussion

Exploring a suitable method for calculations

The structures of **2**, **5** and **5a^{+}**, optimized with MP2/BSS-A, MP2/BSS-B and MP2/BSS-C, were carefully compared with the structures, determined by X-ray crystallography.[30,35] Scheme 1 illustrates the structural parameters of θ (θ_{A} and θ_{B}), d (d_{A} and d_{B}) and the least-square planes σ (σ_{A} and σ_{B}) for the three C atoms bonding to Pn (^{A}Pn or ^{B}Pn) of **1–4** and **5–8**. The d values are defined to be positive and negative, respectively, if Pn are located outside and inside the σ plane with respect to the molecular centre. The "*out*" and "*in*" notations[56] correspond to the positive and negative d values, respectively.

Table 1 Basis set systems (BSSs) employed for the calculations

BSSs	C and H	^{A}Pn, ^{B}Pn and X (= H, F, Cl, Br and I)
BSS-A	Sapporo-TZP + 1s1p	Sapporo-TZP + 1s1p
BSS-B	Sapporo-DZP + 1s1p	Sapporo-TZP + 1s1p
BSS-C	Sapporo-DZP	Sapporo-TZP + 1s1p

Table S1 of the ESI† lists the selected observed and calculated structural parameters for the interaction lengths between ^{A}Pn and ^{B}Pn ($r(^{A}\mathrm{Pn}{-}^{B}\mathrm{Pn})$), θ_{A}, θ_{B}, d_{A} and d_{B}. The differences between the calculated and observed $r(^{A}\mathrm{Pn}{-}^{B}\mathrm{Pn})$ values ($\Delta r(^{A}\mathrm{Pn}{-}^{B}\mathrm{Pn}) = r_{\mathrm{calc}}(^{A}\mathrm{Pn}{-}^{B}\mathrm{Pn}) - r_{\mathrm{obsd}}(^{A}\mathrm{Pn}{-}^{B}\mathrm{Pn})$) are also provided in Table S1.† The $\Delta r(^{A}\mathrm{Pn}{-}^{B}\mathrm{Pn})$ values were 0.027 Å, 0.041 Å and 0.022 Å for **2**, respectively, when calculated with MP2/BSS-A, MP2/BSS-B and MP2/BSS-C. The values were −0.035 Å, −0.024 Å and −0.054 Å for **5**, respectively, if the three methods were applied. The $\Delta r(^{A}\mathrm{Pn}{-}^{B}\mathrm{Pn})$ values were 0.003–0.006 Å for **5a^{+}** by the three methods. The coincidence between the calculated and observed values are excellent for **5a^{+}**.

The MP2/BSS-A method provided excellent quality results; however, the cost performance in the calculations were poorer if the numbers of primitive Gaussian functions necessary for the calculations became larger in **1–8** and **1a^{+}–8e^{+}**. Both MP2/BSS-B and MP2/BSS-C were (very) good with some advantages, whereas disadvantages were for our purpose. We employed MP2/BSS-B since the results with MP2/BSS-B were closer to those with MP2/BSS-A relative to those with MP2/BSS-C. One imaginary frequency was predicted for ^{A}N–H–^{B}N in **1a^{+}**$_{\mathrm{sym}}$ with MP2/BSS-A and MP2/BSS-B, but all real frequencies were predicted with MP2/BSS-C. All real frequencies were predicted for **1a^{+}**$_{\mathrm{nsym}}$ with MP2/BSS-B. The results led us to select MP2/BSS-B for the calculations. The diffuse functions appeared to play an important role in predicting an imaginary frequency around the bridgehead symmetric interactions in **1a^{+}**.

Optimizations and structural features of 1–8 and 1a^{+}–8c^{+}

Optimizations were started assuming the C_{3h} symmetry for **1a^{+}–4e^{+}** and the D_3 symmetry for **5a^{+}–8e^{+}**,[57] although the symmetries were often broken during the optimizations. The minimal structures were optimized with MP2/BSS-B for **1a^{+}–1c^{+}** (X = H, F and Cl), **2a^{+}–4b^{+}** (X = H and F), **5a^{+}–6e^{+}** (X = H, F, Cl, Br and I),

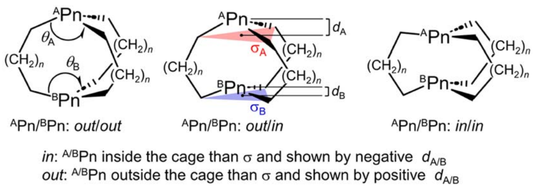

Scheme 1 Selected structural parameters of θ (θ_{A} and θ_{B}) and d (d_{A} and d_{B}) for **1–4** ($n = 1$) and **5–8** ($n = 2$) with the least-square planes σ (σ_{A} and σ_{B}) for the three C atoms bonded to Pn (^{A}Pn and ^{B}Pn). The d values are defined to be positive and negative, respectively, if Pn are located outside and inside the σ plane with respect to the molecular centre. The "*out*" and "*in*" notations correspond to the positive and negative d values, respectively.

$\mathbf{7a^+}$–$\mathbf{7d^+}$ (X = H, F, Cl and Br) and $\mathbf{8a^+}$–$\mathbf{8c^+}$ (X = H, F and Cl). The optimized minimal structures are collectively written as $\mathbf{1a^+}$–$\mathbf{8c^+}$. The optimized minimal structures were only the symmetric shape for $\mathbf{1c^+}$, $\mathbf{4b^+}$, $\mathbf{5c^+}$–$\mathbf{5e^+}$, and $\mathbf{6e^+}$ and only the nonsymmetric shape for $\mathbf{1a^+}$, $\mathbf{5a^+}$ and $\mathbf{7a^+}$, while they were both for $\mathbf{1b^+}$, $\mathbf{2a^+}$, $\mathbf{2b^+}$, $\mathbf{3a^+}$, $\mathbf{3b^+}$, $\mathbf{4a^+}$, $\mathbf{5a^+}$, $\mathbf{5b^+}$, $\mathbf{6a^+}$–$\mathbf{6d^+}$, $\mathbf{7b^+}$–$\mathbf{7d^+}$ and $\mathbf{8a^+}$–$\mathbf{8c^+}$. The difference between ^{A}Sb–H (1.8823 Å) and ^{B}Sb–H (1.8815 Å) in the optimized structure of $\mathbf{4a^+}$ in the C_3 symmetry was negligibly small in magnitude (0.0008 Å); therefore, it could be recognized to have the symmetric shape. The optimizations were not successfully performed for $\mathbf{1e^+}$–$\mathbf{4e^+}$ (X = I). The reason would be the too large size of I$^+$ to incorporate into ^{A}Pn⋯^{B}Pn to give the stable species of $\mathbf{1e^+}$–$\mathbf{4e^+}$. Moreover, the optimizations were successful for those other than above species, but multiple imaginary frequencies were predicted after the frequency analysis. Efforts were made to search the minimal structures for the species. However, the trials were unsuccessful under the calculation conditions. The structures of the symmetric and nonsymmetric shapes are conveniently denoted by $\boldsymbol{mx}^+_{\text{sym}}$ and $\boldsymbol{mx}^+_{\text{nsym}}$ ($\boldsymbol{mx}$ = $\mathbf{1a}$–$\mathbf{8e}$), respectively.

Two types of the transition states (TSs) were optimized. One type appears in the site exchange process between the topological isomers of the nsym shape, where the longer and shorter distances in $^{A/B}$Pn–X–$^{B/A}$Pn are changed. Another type appears between the sym and nsym shapes. While the TSs will be $\boldsymbol{mx}^+_{\text{tp:TS}}$ if the optimized minimal structures are only $\boldsymbol{mx}^+_{\text{nsym}}$, they will be $\boldsymbol{mx}^+_{\text{s–ns:TS}}$ if both $\boldsymbol{mx}^+_{\text{sym}}$ and $\boldsymbol{mx}^+_{\text{nsym}}$ are optimized for a species. No TSs will be optimized for a species if the optimized structure is only $\boldsymbol{mx}^+_{\text{sym}}$. As a result, $\boldsymbol{mx}^+_{\text{tp:TS}}$ will be optimized for $\mathbf{1a^+}$, $\mathbf{5a^+}$ and $\mathbf{7a^+}$, while $\boldsymbol{mx}^+_{\text{s–ns:TS}}$ will appear for $\mathbf{1b^+}$, $\mathbf{2a^+}$, $\mathbf{2b^+}$, $\mathbf{3a^+}$, $\mathbf{3b^+}$, $\mathbf{4a^+}$, $\mathbf{5b^+}$, $\mathbf{6a^+}$–$\mathbf{6d^+}$, $\mathbf{7b^+}$–$\mathbf{7d^+}$ and $\mathbf{8a^+}$–$\mathbf{8c^+}$, under the calculation conditions. Only one imaginary frequency was predicted for each TS. The vibrational motions of TSs corresponding to the imaginary frequencies are shown in Fig. S1 of the ESI,† which confirms the intervention of the TSs between the corresponding two structures. Fig. 1 explains the processes *via* $\boldsymbol{mx}^+_{\text{tp:TS}}$ (a) and $\boldsymbol{mx}^+_{\text{s–ns:TS}}$ (b), exemplified by $\mathbf{5a}^+_{\text{tp:TS}}$ and $\mathbf{6b}^+_{\text{s–ns:TS}}$, respectively. Fig. 1a illustrates the exchange the longer and shorter distances of $^{A/B}$Pn–X–$^{B/A}$Pn in $\mathbf{5a}^+_{\text{nsym}}$ *via* $\mathbf{5a}^+_{\text{tp:TS}}$, where $\mathbf{5a}^+_{\text{nsym}}$ is (very) close to $\mathbf{5a}^+_{\text{tp:TS}}$, since $\mathbf{5a}^+_{\text{nsym}}$ is almost symmetric. Fig. 1b shows the clear exchange of the geometries around ^{A}P and ^{B}P between $\mathbf{6b}^+_{\text{sym}}$ and $\mathbf{6b}^+_{\text{nsym}}$ *via* $\mathbf{6b}^+_{\text{s–ns:TS}}$.

The selected structural parameters optimized with MP2/BSS-B are listed in Table S2 of the ESI;† this table contains the lengths between ^{A}Pn and X ($r(^{A}\text{Pn–X})$) and between ^{B}Pn and X ($r(^{B}\text{Pn–X})$), θ_A, θ_B, d_A, d_B and the types of ^{A}Pn and ^{B}Pn, defined in Scheme 1. The *in*/*in* type was predicted for $\mathbf{1a}^+_{\text{tp:TS}}$, $\mathbf{1a}^+_{\text{nsym}}$, $\mathbf{5a}^+_{\text{tp:TS}}$, $\mathbf{5a}^+_{\text{nsym}}$, $\mathbf{5b}^+_{\text{sym}}$, $\mathbf{5c}^+_{\text{sym}}$, $\mathbf{5d}^+_{\text{sym}}$, $\mathbf{6a}^+_{\text{sym}}$ and $\mathbf{7a}^+_{\text{tp:TS}}$, whereas the *out*/*in* type was for the nonsymmetric shape of $\mathbf{2a^+}$, $\mathbf{5b^+}$, $\mathbf{6a^+}$–$\mathbf{6d^+}$, $\mathbf{7a^+}$–$\mathbf{7c^+}$, $\mathbf{8a^+}$ and $\mathbf{8b^+}$. The *out*/*out* type was optimized for those other than the one listed above. The optimized structures are not shown in the figures, but they can be found in molecular graphs of $\mathbf{1}$–$\mathbf{8}$ and $\mathbf{1a^+}$–$\mathbf{8c^+}$, drawn on the optimized structures with MP2/BSS-B.

The $\Delta r_{\text{Cov}}(^{A/B}\text{Pn–X})$ values for $r(^{A/B}\text{Pn–X})$ of $\mathbf{1a^+}$–$\mathbf{8c^+}$ in the optimized structures were calculated from the sum of the covalent radii[58] ($r_{\text{Cov}}(^{A/B}\text{Pn–X})$). The $\Delta r_{\text{vdW}}(^{A/B}\text{Pn–X})$ values were similarly calculated from the sum of the van der Waals radii[59,60] ($r_{\text{vdW}}(^{A/B}\text{Pn–X})$). The values are listed in Table S2 of the ESI.† Each $r(^{A/B}\text{Pn–X})$ was smaller than the corresponding $r_{\text{vdW}}(^{A/B}\text{Pn–X})$, respectively. The $\Delta r_{\text{Cov}}(^{A/B}\text{Pn–X})$ values were plotted *versus* the species numbers, which was shown in Fig. S2 of the ESI.† Each $r(^{A/B}\text{Pn–X})$ of the symmetric shape was larger than the corresponding $r_{\text{Cov}}(^{A/B}\text{Pn–X})$ ($\Delta r_{\text{Cov}}(^{A/B}\text{Pn–X}) > 0$), respectively, except for $r(^{A/B}\text{Sb–F})$ of $\mathbf{4b}^+_{\text{sym}}$. While $r(^{A}\text{Pn}\cdots\text{X})$ and $r(^{B}\text{Pn–H})$ in each of $\boldsymbol{mx}^+_{\text{nsym}}$ was longer and shorter than the corresponding $r_{\text{Cov}}(\text{Pn–X})$, respectively, with the exception of $r(^{B}\text{N–H})$ in $\mathbf{1a}^+_{\text{nsym}}$ and $\mathbf{5a}^+_{\text{nsym}}$ and $r(^{B}\text{N–F})$ in $\mathbf{1b}^+_{\text{nsym}}$ and $\mathbf{5b}^+_{\text{nsym}}$. The overall order of the lengths was $r(^{A}\text{Pn}\cdots\text{X})_{\text{nsym}} > r(^{A}\text{Pn–X})_{\text{sym}} > r(^{B}\text{Pn–X})_{\text{nsym}}$. While $r(^{A}\text{Pn}\cdots\text{X})_{\text{nsym}}$ and $r(^{A}\text{Pn–X})_{\text{sym}}$ seem noncovalent with the exception of $r(^{A}\text{Sb–F})$ in $\mathbf{4b}^+_{\text{sym}}$, $r(^{B}\text{Pn–X})_{\text{nsym}}$ became covalent with the exception of $r(^{B}\text{N–H})$ of $\mathbf{1a}^+_{\text{nsym}}$ and $\mathbf{5a}^+_{\text{nsym}}$ and $r(^{B}\text{N–F})$ of $\mathbf{1b}^+_{\text{nsym}}$ and $\mathbf{5b}^+_{\text{nsym}}$.

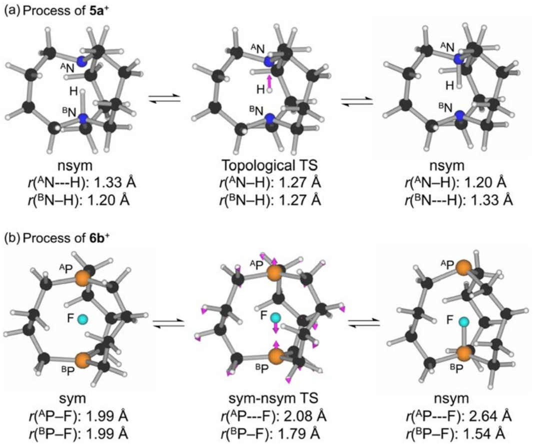

Fig. 1 Processes *via* the TSs of $\boldsymbol{mx}^+_{\text{tp:TS}}$ ($\boldsymbol{mx}$ = 5a) (a) and of $\boldsymbol{mx}^+_{\text{s–ns:TS}}$ ($\boldsymbol{mx}$ = 6b) (b).

Stability of symmetric and nonsymmetric shapes and TSs

The energy values (E: E_{ES} and E_{ZP}) for $\boldsymbol{mx}^+_{\text{sym}}$, $\boldsymbol{mx}^+_{\text{nsym}}$, $\boldsymbol{mx}^+_{\text{s–ns:TS}}$ and/or $\boldsymbol{mx}^+_{\text{tp:TS}}$ ($\boldsymbol{mx}$ = $\mathbf{1a}$–$\mathbf{8e}$) are collected in Table S3 of the ESI,† where E_{ES} and E_{ZP} are E on the energy surface and those corrected with the zero-point energy, respectively. The relative energies (ΔE: ΔE_{ES} and ΔE_{ZP}) are also shown in the table for the species from the global minimum in each group. Each group contains one $\boldsymbol{mx}^+_{\text{sym}}$, one $\boldsymbol{mx}^+_{\text{nsym}}$, one $\boldsymbol{mx}^+_{\text{s–ns:TS}}$ and/or one $\boldsymbol{mx}^+_{\text{tp:TS}}$. A very good correlation was obtained in the plot of ΔE_{ZP} *versus* ΔE_{ES} ($y = -0.73 + 0.93x$, $R_c^2 = 0.991$), as shown in Fig. S3 of the ESI.† As a result, the energy profiles can be discussed using the ΔE_{ES} values.

What are the energies of $\boldsymbol{mx}^+_{\text{sym}}$, $\boldsymbol{mx}^+_{\text{nsym}}$, $\boldsymbol{mx}^+_{\text{s–ns:TS}}$ and/or $\boldsymbol{mx}^+_{\text{tp:TS}}$ ($\boldsymbol{mx}$ = $\mathbf{1a}$–$\mathbf{8c}$), originally? It is instructive to consider the energies of ($\boldsymbol{mx}^+_{\text{sym}}$ and $\boldsymbol{mx}^+_{\text{nsym}}$) from ($\mathbf{1}$–$\mathbf{8}$ and X$^+$). The energy differences correspond to those for the formation of ($\boldsymbol{mx}^+_{\text{sym}}$ and $\boldsymbol{mx}^+_{\text{nsym}}$) from ($\mathbf{1}$–$\mathbf{8}$ and X$^+$); therefore, they are denoted by ΔE_{f} ($\Delta E_{\text{f:ES}}$ and $\Delta E_{\text{f:ZP}}$) ($= E(\boldsymbol{mx}^+) - E(\boldsymbol{mx} + \text{X}^+)$), here. $\Delta E_{\text{f:ES}}$ must strongly reflect the binding energies around the Pn–X–Pn moieties. The ΔE_{f} values are calculated for $\boldsymbol{mx}^+_{\text{sym}}$, $\boldsymbol{mx}^+_{\text{nsym}}$, $\boldsymbol{mx}^+_{\text{s–ns:TS}}$ and/or $\boldsymbol{mx}^+_{\text{tp:TS}}$, which are collected in Table S3 of the ESI.†

Fig. 2 illustrates the $\Delta E_{\mathrm{f:ES}}$ values for the global minimum in each group, $\boldsymbol{mx}^{+}{}_{\mathrm{sym}}$ or $\boldsymbol{mx}^{+}{}_{\mathrm{nsym}}$. The energy levels and arrows are shown in black if $\boldsymbol{mx}^{+}{}_{\mathrm{sym}}$ are the global minima whereas they are in red if $\boldsymbol{mx}^{+}{}_{\mathrm{nsym}}$ is the global minima. Fig. 2 clearly tells us that **1–4** react with H and F to give the stable $\boldsymbol{ma}^{+}$ and $\boldsymbol{mb}^{+}$ (m = 1–4), respectively. The structures are all $\boldsymbol{mx}^{+}{}_{\mathrm{sym}}$ for X = F, while they are all $\boldsymbol{mx}^{+}{}_{\mathrm{nsym}}$ for X = H, except for $\mathbf{4a}^{+}{}_{\mathrm{sym}}$. The cavity size of the bicyclo[3.3.3] system would not be enough large to give the stable moieties of $[\mathrm{Pn–X–Pn}]^{+}$ with X^{+} (X = Cl and Br). Indeed, Cl^{+} reacts with **1** to give $\mathbf{1c}^{+}{}_{\mathrm{sym}}$, but it is less stable than the components by 307 kJ mol^{-1}. The high energy barrier inside the cavity in $\mathbf{1c}^{+}{}_{\mathrm{sym}}$ prevents Cl^{+} to escape from the cavity, irrespective of the less stable property of $\mathbf{1c}^{+}{}_{\mathrm{sym}}$ in energy. It is of interest that H^{+} tends to give $\boldsymbol{mx}^{+}{}_{\mathrm{nsym}}$, whereas F^{+} to $\boldsymbol{mx}^{+}{}_{\mathrm{sym}}$.

Species of **5–8** essentially react with all X^{+} (X = H, F, Cl, Br and I) to give stable species. While **6** (Pn = P) reacts with all X^{+} to give stable species, the adduct of **5** (Pn = N) with I^{+} was optimized but it is less stable than the components. The adduct of **7** (Pn = As) with I^{+} was not optimized; moreover, those of **8** (Pn = Sb) with Br^{+} and I^{+} were not, either. The larger cavities in **5–8** of the bicyclo[4.4.4] system seem superior to the narrower ones in **1–4** of the bicyclo[3.3.3] system to give the stable species in the reaction with X^{+}, especially for X = Br and I. It is also confirmed that the Pn atom affects on the stability of the adducts.

The ΔE_{ES} values for ($\mathbf{1a}^{+}{}_{\mathrm{tp:TS}}$ from $\mathbf{1a}^{+}{}_{\mathrm{nsym}}$) and ($\mathbf{5a}^{+}{}_{\mathrm{tp:TS}}$ from $\mathbf{5a}^{+}{}_{\mathrm{nsym}}$) were predicted to be very small values of 0.02 and 0.04 kJ mol^{-1}, respectively, in magnitudes. Therefore, it would be difficult to distinguish the two structures clearly. The optimized structures of $\boldsymbol{mx}^{+}{}_{\mathrm{tp:TS}}$ ($\boldsymbol{mx}$ = **1a** and **5a**) must be very close to the corresponding $\boldsymbol{mx}^{+}{}_{\mathrm{nsym}}$ (and $\boldsymbol{mx}^{+}{}_{\mathrm{sym}}$) (see Table S3† for **1a** and **5a**). However, ΔE_{ES} for $\mathbf{7a}^{+}{}_{\mathrm{tp:TS}}$ from $\mathbf{7a}^{+}{}_{\mathrm{nsym}}$ were predicted to be very large value of 76.2 kJ mol^{-1}. $\mathbf{7a}^{+}{}_{\mathrm{tp:TS}}$ must be substantially different from $\mathbf{7a}^{+}{}_{\mathrm{nsym}}$. The optimized structure of $\mathbf{7a}^{+}{}_{\mathrm{tp:TS}}$ seems symmetric. The differences between Pn = As in $\mathbf{7a}^{+}$ and Pn = N in $\mathbf{1a}^{+}$ and $\mathbf{5a}^{+}$ would be responsible for the results.

Fig. 3 shows the relative values of ΔE_{ES} ($\boldsymbol{mx}^{+}{}_{\mathrm{sym}}$), ΔE_{ES} ($\boldsymbol{mx}^{+}{}_{\mathrm{s–ns:TS}}$) and ΔE_{ES} ($\boldsymbol{mx}^{+}{}_{\mathrm{nsym}}$) from the global minimum of each group. As a result, all ΔE_{ES} ($\boldsymbol{mx}^{+}$) are plotted upside of the corresponding global minimum. The energy levels and the model lines for the reaction coordinates are illustrated in black if ΔE_{ES} ($\boldsymbol{mx}^{+}{}_{\mathrm{sym}}$) < ΔE_{ES} ($\boldsymbol{mx}^{+}{}_{\mathrm{nsym}}$), whereas they are in red when ΔE_{ES} ($\boldsymbol{mx}^{+}{}_{\mathrm{sym}}$) > ΔE_{ES} ($\boldsymbol{mx}^{+}{}_{\mathrm{nsym}}$). The colors in Fig. 2 and 3 are related to each other. Only one plot in black appeared for each of $\mathbf{1b}^{+}$, $\mathbf{4a}^{+}$ and $\mathbf{5b}^{+}$; therefore, the plots are shown as Fig. 3a. The plots for ($\mathbf{2a}^{+}$ and $\mathbf{2b}^{+}$), ($\mathbf{3a}^{+}$ and $\mathbf{3b}^{+}$), ($\mathbf{6a}^{+}$–$\mathbf{6d}^{+}$), ($\mathbf{7b}^{+}$–$\mathbf{7d}^{+}$) and ($\mathbf{8a}^{+}$–$\mathbf{8c}^{+}$) are drawn in Fig. 3b–f, respectively.

The ΔE_{ES} values for ($\mathbf{1b}^{+}{}_{\mathrm{nsym}}$ and $\mathbf{1b}^{+}{}_{\mathrm{s–ns:TS}}$ from $\mathbf{1b}^{+}{}_{\mathrm{sym}}$), ($\mathbf{4a}^{+}{}_{\mathrm{nsym}}$ and $\mathbf{4a}^{+}{}_{\mathrm{s–ns:TS}}$ from $\mathbf{4a}^{+}{}_{\mathrm{sym}}$), and ($\mathbf{5b}^{+}{}_{\mathrm{nsym}}$ and $\mathbf{5b}^{+}{}_{\mathrm{s–ns:TS}}$ from $\mathbf{5b}^{+}{}_{\mathrm{sym}}$) were predicted to be (70.7 and 72.7 kJ mol^{-1}), (10.0 and 14.8 kJ mol^{-1}) and (91.9 and 95.3 kJ mol^{-1}), respectively, in magnitudes. The results are illustrated in Fig. 3a with the ΔE_{ES} values. Similarly, the calculated ΔE_{ES} values for $\boldsymbol{mx}^{+}{}_{\mathrm{nsym}}$ and $\boldsymbol{mx}^{+}{}_{\mathrm{s–ns:TS}}$ from $\boldsymbol{mx}^{+}{}_{\mathrm{sym}}$ ($\boldsymbol{mx}^{+}$ = $\mathbf{2a}^{+}$–$\mathbf{8c}^{+}$) are drawn in Fig. 3b–f, respectively.

Fig. 2 and 3 are illustrated in such a way that all processes can be visualized for the formation of $\boldsymbol{mx}^{+}{}_{\mathrm{sym}}$, $\boldsymbol{mx}^{+}{}_{\mathrm{nsym}}$, $\boldsymbol{mx}^{+}{}_{\mathrm{s–ns:TS}}$ and $\boldsymbol{mx}^{+}{}_{\mathrm{tp:TS}}$ ($\boldsymbol{mx}$ = **1a–8c**) from the components, **1–8** and X^{+} (X = H, F, Cl, Br and I), by overlapping the energy levels of the common species in the two figures. While the red lines should connect to the red ones, the black lines to the black ones, in this process. The $\Delta E_{\mathrm{f:ES}}$ values for all species are obtained by adding the values along the processes *via* the global minimum in a group. (The memory widths on the vertical axes are different.) The ΔE_{ES} values are given in the figures, which are also found in Table S3 of the ESI.†

The ΔE_{ES} values for both $\boldsymbol{mx}^{+}{}_{\mathrm{nsym}}$ and $\boldsymbol{mx}^{+}{}_{\mathrm{s–ns:TS}}$ increase in the order of Pn = P (in $\mathbf{6c}^{+}$) < As (in $\mathbf{7c}^{+}$) < Sb (in $\mathbf{8c}^{+}$). However, the orders for others are unclear, since some data are lacking due to unsuccessful optimizations and some disorders seem to occur. In the case of $\mathbf{6b}^{+}$–$\mathbf{6d}^{+}$ and $\mathbf{7b}^{+}$–$\mathbf{7d}^{+}$, the ΔE_{ES} values for $\boldsymbol{mx}^{+}{}_{\mathrm{nsym}}$ increase in the order of X = F < Cl < Br whereas the values for $\boldsymbol{mx}^{+}{}_{\mathrm{s–ns:TS}}$ decreased in the order of X = F > Cl > Br. The opposite trends between $\boldsymbol{mx}^{+}{}_{\mathrm{nsym}}$ and $\boldsymbol{mx}^{+}{}_{\mathrm{s–ns:TS}}$ are of interest. The similar trend was detected in $\mathbf{8b}^{+}{}_{\mathrm{nsym}}$ and $\mathbf{8c}^{+}{}_{\mathrm{nsym}}$, of which ΔE_{ES} values increased in the order of X = F < Cl.

The $^{\mathrm{A}}\mathrm{Pn–X–}^{\mathrm{B}}\mathrm{Pn}$ and/or $^{\mathrm{A}}\mathrm{Pn}\cdots\mathrm{X–}^{\mathrm{B}}\mathrm{Pn}$ interactions plays an important role in stabilising the symmetric and nonsymmetric shapes of $\mathbf{1a}^{+}$–$\mathbf{8c}^{+}$, respectively, together with the TSs, although the contributions seem complex. The secondary interactions also contribute to control the fine details of the structures.

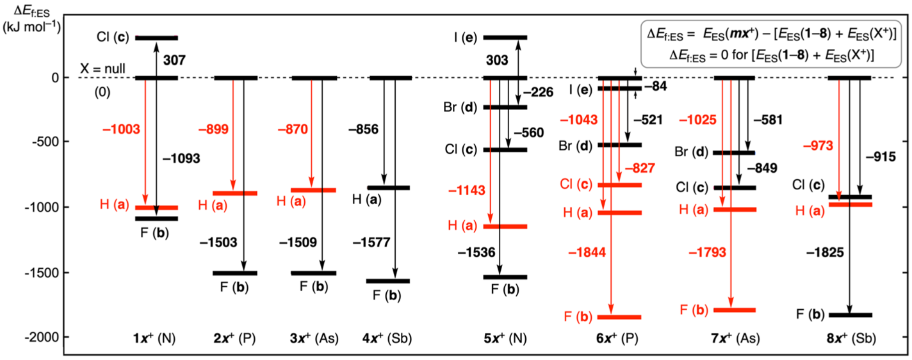

Fig. 2 Energy profiles for the formation of $\boldsymbol{mx}^{+}{}_{\mathrm{sym}}$ and/or $\boldsymbol{mx}^{+}{}_{\mathrm{nsym}}$ of the minimal structures from **1–8** and X^{+} (X = H, F, Cl, Br and I), optimized with MP2/BSS-B. The energy of each combination of **1–8** and X^{+} was taken as the standard for each energy producing $\boldsymbol{mx}^{+}{}_{\mathrm{sym}}$ and/or $\boldsymbol{mx}^{+}{}_{\mathrm{nsym}}$, which are given in kJ mol^{-1}. The energy levels and the values are described in black for $\boldsymbol{mx}^{+}{}_{\mathrm{sym}}$, whereas they are given in red for $\boldsymbol{mx}^{+}{}_{\mathrm{nsym}}$ in the diagram.

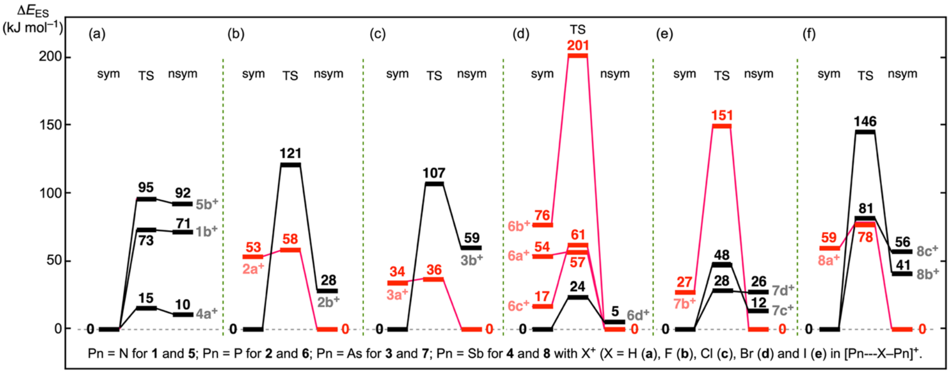

Fig. 3 Plots of ΔE_{ES} ($\boldsymbol{mx}^{+}_{\mathrm{sym}}$), ΔE_{ES} ($\boldsymbol{mx}^{+}_{\mathrm{s-ns:TS}}$) and ΔE_{ES} ($\boldsymbol{mx}^{+}_{\mathrm{nsym}}$), optimized with MP2/BSS-B. Plots are for **1b**$^+$, **4a**$^+$ and **5b**$^+$ (a), **2a**$^+$ and **2b**$^+$ (b), **3a**$^+$ and **3b**$^+$ (c), **6a**$^+$–**6d**$^+$ (d), **7b**$^+$–**7d**$^+$ (e) and **8a**$^+$–**8c**$^+$ (f). The energy levels and the model lines for the reaction coordinates are illustrated in black when ΔE_{ES} ($\boldsymbol{mx}^{+}_{\mathrm{sym}}$) < ΔE_{ES} ($\boldsymbol{mx}^{+}_{\mathrm{nsym}}$) and in red if ΔE_{ES} ($\boldsymbol{mx}^{+}_{\mathrm{sym}}$) > ΔE_{ES} ($\boldsymbol{mx}^{+}_{\mathrm{nsym}}$).

Molecular graphs with contour plots for 1–8 and 1a$^+$–8c$^+$

Fig. 4 shows the molecular graphs with contour plots drawn on the selected minimal structures of **1a**$^+$–**8c**$^+$, optimized with MP2/BSS-B. Those of others, containing those for **1**–**8**, are shown in Fig. S4–S6 of the ESI.† The BCPs corresponding to the $^{\mathrm{A}}$Pn⋯$^{\mathrm{B}}$Pn interactions were detected for $^{\mathrm{A}}$N-*-$^{\mathrm{B}}$N in **1** and **5** and $^{\mathrm{A}}$P-*-$^{\mathrm{B}}$P in **6**, although such BCPs were not detected for **2**–**4**, **7** and **8**, due to the clear *out*/*out* structures with the large $^{\mathrm{A}}$Pn⋯$^{\mathrm{B}}$Pn distances for **7** and **8** (see Table S2 of the ESI†). The BCPs were detected for $^{\mathrm{A}}$Pn–X–$^{\mathrm{B}}$Pn in **1a**$^+$–**8c**$^+$, along with those for the secondary H-*-H and X-*-C interactions in **2**–**8** and **1b**$^+$–**8c**$^+$, together with that for H-*-$^{\mathrm{B}}$Sb in **8a**$^{+}_{\mathrm{sym}}$.

The BPs in $^{\mathrm{A}}$Pn–*–$^{\mathrm{B}}$Pn and $^{\mathrm{A}}$Pn-*-X appeared straight, as shown in Fig. 4 and S4–S6 of the ESI.† What is the linearity of the BPs for $^{\mathrm{A}}$Pn–*–$^{\mathrm{B}}$Pn and Pn-*-X? The lengths of BPs (r_{BP}) and the straight-line distances (R_{SL}) corresponding to r_{BP} of $^{\mathrm{A}}$Pn–*–$^{\mathrm{B}}$Pn in **1**, **5** and **6** and Pn-*-X in **1a**$^+$–**8c**$^+$ are listed in Table S4 of the ESI,† along with the differences between r_{BP} and R_{SL}, Δr_{BP} (= $r_{\mathrm{BP}} - R_{\mathrm{SL}}$). The $^{\mathrm{A}}$Pn–*–$^{\mathrm{B}}$Pn and Pn-*-X interactions in **1**, **5**, **6** and **1a**$^+$–**8c**$^+$ were recognized to be straight, since the Δr_{BP} values were less than 0.01 Å. However, the BPs for H–*–H and H–*–$^{\mathrm{B}}$Sb in **8a**$^{+}_{\mathrm{nsym}}$ and some X–*–C were bent compared with those of $^{\mathrm{A}}$Pn–*–$^{\mathrm{B}}$Pn and Pn-*-X, of which Δr_{BP} values are provided in Table S5 of the ESI.† The Δr_{BP} values were 0.02–0.23 Å for H–*–H, H–*–$^{\mathrm{B}}$Sb in **8a**$^{+}_{\mathrm{nsym}}$, Cl–*–C in **6c**$^{+}_{\mathrm{nsym}}$, Br–*–C in **6d**$^{+}_{\mathrm{sym}}$ and **6d**$^{+}_{\mathrm{nsym}}$, I–*–C in **6e**$^{+}_{\mathrm{sym}}$, and F–*–C in **7b**$^{+}_{\mathrm{nsym}}$, **8b**$^{+}_{\mathrm{sym}}$ and **8b**$^{+}_{\mathrm{nsym}}$. For other X–*–C, the Δr_{BP} values were less than 0.20 Å; thus, they were approximately straight.

The values of $\rho_{\mathrm{b}}(\boldsymbol{r}_{\mathrm{c}})$, $V_{\mathrm{b}}(\boldsymbol{r}_{\mathrm{c}})$, $G_{\mathrm{b}}(\boldsymbol{r}_{\mathrm{c}})$ and $H_{\mathrm{b}}(\boldsymbol{r}_{\mathrm{c}})$, which were called the QTAIM functions here, were calculated at the BCPs that appeared in molecular graphs, as shown in Fig. 4, for example. Table 2 lists the values of the QTAIM functions of $\rho_{\mathrm{b}}(\boldsymbol{r}_{\mathrm{c}})$, $H_{\mathrm{b}}(\boldsymbol{r}_{\mathrm{c}}) - V_{\mathrm{b}}(\boldsymbol{r}_{\mathrm{c}})/2$ and $H_{\mathrm{b}}(\boldsymbol{r}_{\mathrm{c}})$, evaluated with MP2/BSS-B.

Intrinsic dynamic and static natures of $^{\mathrm{A}}$Pn-*-X and $^{\mathrm{B}}$Pn-*-X in 1a$^+$–8c$^+$, elucidated with QTAIM-DFA

The natures of the interactions in question in the optimized minimal species are mainly discussed in this section. Fig. 5 shows the QTAIM-DFA plots of $H_{\mathrm{b}}(\boldsymbol{r}_{\mathrm{c}})$ *versus* $H_{\mathrm{b}}(\boldsymbol{r}_{\mathrm{c}}) - V_{\mathrm{b}}(\boldsymbol{r}_{\mathrm{c}})/2$, although the data are limited to those for $^{\mathrm{A/B}}$Pn-*-X in $\boldsymbol{mx}^{+}_{\mathrm{sym}}$ (see Table 2 for the data), while those for $^{\mathrm{A}}$Pn–*–X and $^{\mathrm{B}}$Pn-*-X in $\boldsymbol{mx}^{+}_{\mathrm{nsym}}$ are shown in Fig. S7 of the ESI.† Data from the perturbed structures generated with CIV are also employed for the plot. The 17 (data) points appeared in the SS region. While the plots for others than those above appeared in the *r*-CS region, except for three, which appeared in the *p*-CS region (see Fig. 5 and S7 of the ESI† for the interactions and the species). The results imply that $^{\mathrm{A}}$Pn-*-X, $^{\mathrm{A}}$Pn–*–X and $^{\mathrm{B}}$Pn-*-X show various natures of the wide ranges over the *p*-CS to SS regions.

The plots were analysed according to eqn (SA3)–(SA6) of the ESI.† (See the appendix in the ESI for eqn (SA3)–(SA6) and Fig. SA1†). The θ values of 180° < θ < 206.6° correspond to the shared-shell (SS) interactions of $H_{\mathrm{b}}(\boldsymbol{r}_{\mathrm{c}}) - V_{\mathrm{b}}(\boldsymbol{r}_{\mathrm{c}})/2 < 0$, and the values less than 180° (θ < 180°) do to the closed-shell (CS) interactions of $H_{\mathrm{b}}(\boldsymbol{r}_{\mathrm{c}}) - V_{\mathrm{b}}(\boldsymbol{r}_{\mathrm{c}})/2 > 0$. The CS interactions are subdivided into regular CS (*r*-CS) interactions by 90° < θ < 180° ($H_{\mathrm{b}}(\boldsymbol{r}_{\mathrm{c}}) < 0$ and $H_{\mathrm{b}}(\boldsymbol{r}_{\mathrm{c}}) - V_{\mathrm{b}}(\boldsymbol{r}_{\mathrm{c}})/2 > 0$) and pure CS (*p*-CS) interactions by 45° < θ < 90° ($H_{\mathrm{b}}(\boldsymbol{r}_{\mathrm{c}}) > 0$ and $H_{\mathrm{b}}(\boldsymbol{r}_{\mathrm{c}}) - V_{\mathrm{b}}(\boldsymbol{r}_{\mathrm{c}})/2 > 0$). The classical covalent interactions (Cov) of SS are subdivided by R into strong (Cov-s: R > 0.15 au) and weak (Cov-w: R < 0.15 au).

While the typical HB (*t*-HB) nature with covalency (*t*-HB$_{\mathrm{wc}}$), molecular complex formation through CT (CT-MC), and TBP adduct formation through CT (CT-TBP) are contained in *r*-CS, the *t*-HB nature with no covalency (*t*-HB$_{\mathrm{nc}}$) and van der Waals interactions (vdW) belong to *p*-CS. The nature of each Pn-*-X interaction in **1a**$^+$–**8c**$^+$ was classified and characterized with the QTAIM-DFA parameters of (R, θ, θ_{p}), employing the criteria as guidance. Table 2 lists the analysed QTAIM-DFA parameters of (R, θ) and (θ_{p}, κ_{p}), along with the C_{ii} values, corresponding to generate the perturbed structures, evaluated with MP2/BSS-B. Table 2 also provides the intrinsic dynamic and static natures predicted for the interactions.

After careful examination of (θ, θ_{p}) for standard interactions, the borderlines between the CS interactions were determined as follows: The (θ, θ_{p}) values of (75°, **90°**), (**90°**, 125°), (115°, **150°**), (150°, **180°**) and (**180°**, 190°) correspond to the borderlines between vdW/*t*-HB$_{\mathrm{nc}}$, *t*-HB$_{\mathrm{nc}}$/*t*-HB$_{\mathrm{wc}}$, *t*-HB$_{\mathrm{wc}}$/CT-MC, CT-MC/CT-TBP and CT-TBP/Cov-w, respectively. The parameters in bold

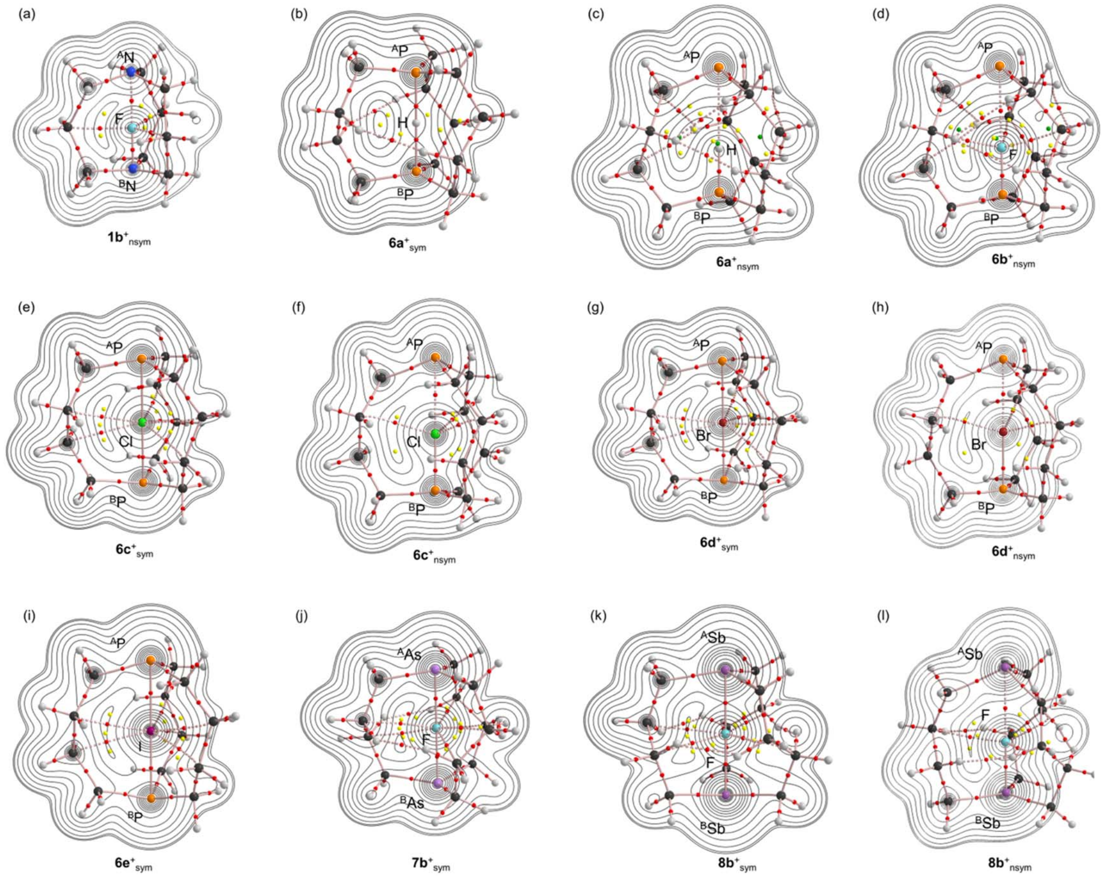

Fig. 4 Molecular graphs with contour plots for $\mathbf{1b}^{+}_{\rm nsym}$, $\mathbf{6a}^{+}_{\rm sym}$, $\mathbf{6a}^{+}_{\rm nsym}$, $\mathbf{6b}^{+}_{\rm nsym}$, $\mathbf{6c}^{+}_{\rm sym}$, $\mathbf{6c}^{+}_{\rm nsym}$, $\mathbf{6d}^{+}_{\rm sym}$, $\mathbf{6d}^{+}_{\rm nsym}$, $\mathbf{6e}^{+}_{\rm sym}$, $\mathbf{7b}^{+}_{\rm sym}$, $\mathbf{8b}^{+}_{\rm sym}$ and $\mathbf{8b}^{+}_{\rm nsym}$ ((a)–(l), respectively), calculated with MP2/BSS-B. The BCPs are denoted by red dots, RCPs (ring critical points) by yellow dots, CCPs (cage critical points) by green dots and BPs by pink lines. Carbon, hydrogen, nitrogen, phosphorus, arsenic, antimony, fluorine, chlorine, bromine and iodine atoms are shown in black, grey, blue, orange, light purple, purple, light green, green, dark red and dark purple, respectively. Contour plots are drawn on the planes containing at least $^{\rm A}$Pn, $^{\rm B}$Pn and X.

are superior to those in plain font in the prediction of the natures, while those in plain font are provided as tentative ones.

While θ classifies the interactions, $\theta_{\rm p}$ characterizes them. The (R, θ, $\theta_{\rm p}$) values are (0.162–0.332 au, 182.4–199.6°, 128.3–206.6°), for $^{\rm A}$N–*–H and $^{\rm B}$N-*-H ($\mathbf{1a}^{+}_{\rm nsym}$), $^{\rm B}$N-*-F ($\mathbf{1b}^{+}_{\rm nsym}$ and $\mathbf{5b}^{+}_{\rm nsym}$), $^{\rm B}$P-*-H ($\mathbf{2a}^{+}_{\rm nsym}$ and $\mathbf{6a}^{+}_{\rm nsym}$), $^{\rm B}$N-*-H ($\mathbf{5a}^{+}_{\rm nsym}$) and $^{\rm B}$P-*-Br ($\mathbf{6d}^{+}_{\rm nsym}$); therefore, the interactions are predicted to have the SS/Cov-s nature. Similarly, the (R, θ, $\theta_{\rm p}$) values were (0.040–0.147 au, 181.8–197.2°, 168.3–206.0°) for $^{\rm A/B}$P-*-H ($\mathbf{2a}^{+}_{\rm sym}$ and $\mathbf{6a}^{+}_{\rm nsym}$), $^{\rm A/B}$As-*-H ($\mathbf{3a}^{+}_{\rm sym}$), $^{\rm B}$As-*-H ($\mathbf{3a}^{+}_{\rm nsym}$ and $\mathbf{7a}^{+}_{\rm nsym}$), $^{\rm A}$N–*–H ($\mathbf{5a}^{+}_{\rm nsym}$), $^{\rm A/B}$P-*-Cl ($\mathbf{6c}^{+}_{\rm sym}$), $^{\rm A/B}$P-*-Br ($\mathbf{6d}^{+}_{\rm sym}$), $^{\rm A/B}$P-*-I ($\mathbf{6e}^{+}_{\rm sym}$) and $^{\rm B}$As-*-Br ($\mathbf{7d}^{+}_{\rm nsym}$); thus, these were predicted to be the SS/Cov-w nature. In the case of CS interactions, the *r*-CS/CT-TBP nature was predicted for $^{\rm A/B}$N-*-Cl ($\mathbf{1c}^{+}_{\rm sym}$ and $\mathbf{5c}^{+}_{\rm sym}$), $^{\rm A}$P–*–H ($\mathbf{2a}^{+}_{\rm nsym}$), $^{\rm A}$As–*–H ($\mathbf{3a}^{+}_{\rm nsym}$), $^{\rm A/B}$N-*-Br ($\mathbf{5d}^{+}_{\rm sym}$), $^{\rm A/B}$P-*-F ($\mathbf{6b}^{+}_{\rm sym}$), $^{\rm A}$P–*–Br ($\mathbf{6d}^{+}_{\rm nsym}$) and $^{\rm A}$As–*–Br ($\mathbf{7d}^{+}_{\rm nsym}$), of which the ($\theta$, $\theta_{\rm p}$) values were (134.2–177.3°, 180.8–198.7°). The *r*-CS/CT-MC nature was predicted for $^{\rm A/B}$N-*-F ($\mathbf{1b}^{+}_{\rm sym}$), $^{\rm A}$P–*–F ($\mathbf{2b}^{+}_{\rm nsym}$), $^{\rm A}$Sb–*–H/$^{\rm B}$Sb-*-H ($\mathbf{4a}^{+}_{\rm nsym}$ and $\mathbf{8a}^{+}_{\rm nsym}$), $^{\rm A}$P–*–Cl ($\mathbf{6c}^{+}_{\rm nsym}$), $^{\rm A}$As–*–H ($\mathbf{7a}^{+}_{\rm nsym}$), $^{\rm A/B}$As-*-Cl ($\mathbf{7c}^{+}_{\rm sym}$), $^{\rm A}$As–*–Cl/$^{\rm B}$As-*-Cl ($\mathbf{7c}^{+}_{\rm nsym}$), $^{\rm A/B}$As-*-Br ($\mathbf{7d}^{+}_{\rm sym}$), $^{\rm A/B}$Sb-*-H ($\mathbf{8a}^{+}_{\rm sym}$) and $^{\rm A}$Sb–*–Cl ($\mathbf{8c}^{+}_{\rm nsym}$), due to the ($\theta$, $\theta_{\rm p}$) values of (99.7–176.3°, 153.0–176.5°).

The *r*-CS/*t*-HB$_{\rm wc}$ nature was predicted for $^{\rm A}$N–*–F ($\mathbf{1b}^{+}_{\rm nsym}$ and $\mathbf{5b}^{+}_{\rm nsym}$), $^{\rm A/B}$P-*-F ($\mathbf{2b}^{+}_{\rm sym}$), $^{\rm B}$P-*-F ($\mathbf{2b}^{+}_{\rm nsym}$ and $\mathbf{6b}^{+}_{\rm nsym}$), $^{\rm A/B}$As-*-F ($\mathbf{3b}^{+}_{\rm sym}$ and $\mathbf{7b}^{+}_{\rm sym}$), $^{\rm A}$As–*–F ($\mathbf{3b}^{+}_{\rm nsym}$), $^{\rm B}$As-*-F ($\mathbf{3b}^{+}_{\rm nsym}$ and $\mathbf{7b}^{+}_{\rm nsym}$), $^{\rm A/B}$Sb-*-H ($\mathbf{4a}^{+}_{\rm sym}$), $^{\rm A/B}$Sb-*-F ($\mathbf{4b}^{+}_{\rm sym}$ and $\mathbf{8b}^{+}_{\rm sym}$), $^{\rm A/B}$N-*-F ($\mathbf{5b}^{+}_{\rm sym}$), $^{\rm A/B}$N-*-I ($\mathbf{5b}^{+}_{\rm sym}$), $^{\rm A}$P–*–H ($\mathbf{6a}^{+}_{\rm nsym}$), $^{\rm B}$P-*-Cl ($\mathbf{6c}^{+}_{\rm nsym}$), $^{\rm B}$Sb-*-F ($\mathbf{8b}^{+}_{\rm nsym}$), $^{\rm A/B}$Sb-*-Cl ($\mathbf{8c}^{+}_{\rm sym}$) and $^{\rm B}$Sb-*-Cl ($\mathbf{8c}^{+}_{\rm nsym}$), of which ($\theta$, $\theta_{\rm p}$) values were (92.5–175.9°, 99.8–149.6°). The (θ, $\theta_{\rm p}$) values for $^{\rm A}$P–*–F ($\mathbf{6b}^{+}_{\rm nsym}$), $^{\rm A}$As–*–F ($\mathbf{7b}^{+}_{\rm nsym}$) and $^{\rm A}$Sb–*–F ($\mathbf{8b}^{+}_{\rm nsym}$) were (78.9–84.3°, 91.0–102.6°); thus, they were predicted to be the *p*-CS/*t*-HB$_{\rm nc}$ nature.

The differences between θ and $\theta_{\rm p}$ ($\Delta\theta_{\rm p} = \theta_{\rm p} - \theta$) are positive for usual interactions, which show normal behaviour. However, the $\Delta\theta_{\rm p}$ values are sometimes negative, which show inverse behaviour. The inverse *versus* normal behaviour of interactions in relation to the $\Delta\theta_{\rm p}$ values, which we proposed recently, would correspond to some basic properties of interactions.[61] The inverse behaviour is often observed when the interaction occurs between the atoms, of which atomic numbers are (very) large. Such cases can be easily found in Table 2. The abnormal character of $G_{\rm b}(\mathbf{r}_{\rm c})$ at the BCP for the interactions seems responsible for the inverse behaviour.

Table 2 QTAIM functions and QTAIM-DFA parameters of **A/BPn-*-X,** $^{\text{A}}$Pn–*–X and/or $^{\text{B}}$Pn-*-X for **1a**$^+$–**8c**$^+$, together with the C_{ii} values and the predicted natures, evaluated with MP2/BSS-B^{a,b}

mx$^{+}_{\text{sym/nsym (symmetry)}}$ ($^{\text{A/B}}$Pn-*-X)	$\rho_{\text{b}}(\boldsymbol{r}_{\text{c}})$ ($ea_{\text{o}}{}^{-3}$)	$c\nabla^2\rho_{\text{b}}(\boldsymbol{r}_{\text{c}})^c$ (au)	$H_{\text{b}}(\boldsymbol{r}_{\text{c}})$ (au)	R^d (au)	θ^e (°)	$C_{ii}{}^f$ (Å mdyn^{-1})	$\theta_{\text{p}}{}^g$ (°)	$\kappa_{\text{p}}{}^h$ (au^{-1})	Predicted nature
1a$^{+}_{\text{nsym}}$ (C_1) ($^{\text{A}}$N–*–H)	0.1815	−0.0445	−0.1805	0.1859	193.9	19.19	205.2	0.1	SS/Cov-s
($^{\text{B}}$N-*-H)	0.2364	−0.1009	−0.2959	0.3126	198.8	12.80	206.6	0.0	SS/Cov-s
1b$^{+}_{\text{sym}}$ ($C_{3\text{h}}$) ($^{\text{A/B}}$N-*-F)	0.1518	0.0626	−0.0590	0.0860	133.3	0.155	155.0	7.4	*r*-CS/CT-MC
1b$^{+}_{\text{nsym}}$ (C_3) ($^{\text{A}}$N–*–F)	0.0860	0.0520	−0.0155	0.0543	106.6	0.506	146.5	20.1	*r*-CS/*t*-HB$_{\text{wc}}$
($^{\text{B}}$N-*-F)	0.3334	−0.0212	−0.3316	0.3323	183.7	0.302	199.0	0.1	SS/Cov-s
1c$^{+}_{\text{sym}}$ ($C_{3\text{h}}$) ($^{\text{A}}$N-*-Cl)	0.1790	0.0087	−0.1148	0.1151	175.6	0.547	196.2	1.0	*r*-CS/CT-TBP
2a$^{+}_{\text{sym}}$ ($C_{3\text{h}}$) ($^{\text{A/B}}$P-*-H)	0.1088	−0.0180	−0.0709	0.0732	194.2	0.613	198.5	2.2	SS/Cov-w
2a$^{+}_{\text{nsym}}$ (C_3) ($^{\text{A}}$P–*–H)	0.0464	0.0098	−0.0108	0.0146	137.7	0.860	182.7	28.9	*r*-CS/CT-TBP
($^{\text{B}}$P-*-H)	0.1980	−0.0091	−0.2209	0.2211	182.4	0.238	128.3	1.7	SS/Cov-s
2b$^{+}_{\text{sym}}$ ($C_{3\text{h}}$) ($^{\text{A/B}}$P-*-F)	0.0968	0.0237	−0.0645	0.0687	159.8	0.247	116.8	39.8	*r*-CS/*t*-HB$_{\text{wc}}$
2b$^{+}_{\text{nsym}}$ (C_3) ($^{\text{A}}$P–*–F)	0.0455	0.0230	−0.0039	0.0234	99.7	0.480	157.6	79.2	*r*-CS/CT-MC
($^{\text{B}}$P-*-F)	0.1987	0.1707	−0.1335	0.2167	128.0	0.125	106.4	0.1	*r*-CS/*t*-HB$_{\text{wc}}$
3a$^{+}_{\text{sym}}$ ($C_{3\text{h}}$) ($^{\text{A/B}}$As-*-H)	0.0924	−0.0047	−0.0487	0.0489	185.6	0.800	187.1	4.0	SS/Cov-w
3a$^{+}_{\text{nsym}}$ (C_3) ($^{\text{A}}$As–*–H)	0.0438	0.0089	−0.0101	0.0134	138.7	0.981	180.8	21.5	*r*-CS/CT-TBP
($^{\text{B}}$As-*-H)	0.1800	−0.0177	−0.1457	0.1468	186.9	0.279	168.6	2.4	SS/Cov-w
3b$^{+}_{\text{sym}}$ ($C_{3\text{h}}$) ($^{\text{A/B}}$As-*-F)	0.0918	0.0404	−0.0321	0.0516	128.5	0.267	123.2	0.7	*r*-CS/*t*-HB$_{\text{wc}}$
3b$^{+}_{\text{nsym}}$ (C_3) ($^{\text{A}}$As–*–F)	0.0431	0.0213	−0.0036	0.0216	99.6	0.584	140.7	22.0	*r*-CS/*t*-HB$_{\text{wc}}$
($^{\text{B}}$As-*-F)	0.1848	0.1156	−0.1202	0.1668	136.1	0.154	128.8	1.4	*r*-CS/*t*-HB$_{\text{wc}}$
4a$^{+}_{\text{sym}}$ (C_3) ($^{\text{A/B}}$Sb-*-H)^i	0.0764	0.0084	−0.0305	0.0316	164.5	0.646	148.9	4.9	*r*-CS/*t*-HB$_{\text{wc}}$
4a$^{+}_{\text{nsym}}$ (C_3) ($^{\text{A}}$Sb–*–H)	0.0409	0.0076	−0.0097	0.0123	142.0	1.174	169.6	15.4	*r*-CS/CT-MC
($^{\text{B}}$Sb-*-H)	0.1308	0.0123	−0.0744	0.0754	170.6	0.435	158.1	1.4	*r*-CS/CT-MC
4b$^{+}_{\text{sym}}$ ($C_{3\text{h}}$) ($^{\text{A/B}}$Sb-*-F)^j	0.0856	0.0654	−0.0111	0.0663	99.7	0.282	109.3	164.4	*r*-CS/*t*-HB$_{\text{wc}}$
5a$^{+}_{\text{nsym}}$ (C_3) ($^{\text{A}}$N–*–H)	0.1491	−0.0306	−0.1291	0.1327	193.3	10.36	204.6	0.2	SS/Cov-w
($^{\text{B}}$N-*-H)	0.2108	−0.0895	−0.2519	0.2673	199.6	6.953	206.1	0.0	SS/Cov-s
5b$^{+}_{\text{sym}}$ (D_3) ($^{\text{A/B}}$N-*-F)	0.1116	0.0487	−0.0264	0.0554	118.5	0.305	148.0	9.8	*r*-CS/*t*-HB$_{\text{wc}}$
5b$^{+}_{\text{nsym}}$ (C_3) ($^{\text{A}}$N–*–F)	0.0542	0.0330	−0.0015	0.0331	92.5	1.156	128.4	30.8	*r*-CS/*t*-HB$_{\text{wc}}$
($^{\text{B}}$N-*-F)	0.3091	−0.0186	−0.2833	0.2839	183.8	0.284	197.7	0.0	SS/Cov-s
5c$^{+}_{\text{sym}}$ (C_3) ($^{\text{A/B}}$N-*-Cl)	0.1722	0.0049	−0.1042	0.1043	177.3	0.424	194.3	1.6	*r*-CS/CT-TBP
5d$^{+}_{\text{sym}}$ (C_2) ($^{\text{A}}$N-*-Br)	0.1508	0.0072	−0.0963	0.0966	175.7	0.405	186.5	2.2	*r*-CS/CT-TBP
5e$^{+}_{\text{sym}}$ (D_3) ($^{\text{A}}$N-*-I)	0.1262	0.0225	−0.0729	0.0763	162.8	0.403	149.6	14.8	*r*-CS/*t*-HB$_{\text{wc}}$
6a$^{+}_{\text{sym}}$ (C_2) ($^{\text{A/B}}$P-*-H)	0.1242	−0.0228	−0.0736	0.0771	197.2	2.470	206.0	0.1	SS/Cov-w
6a$^{+}_{\text{nsym}}$ (C_2) ($^{\text{A}}$P–*–H)	0.0161	0.0048	−0.0003	0.0048	93.9	3.611	134.2	260.5	*r*-CS/*t*-HB$_{\text{wc}}$
($^{\text{B}}$P-*-H)	0.1857	−0.0217	−0.2041	0.2053	186.1	0.269	129.7	2.6	SS/Cov-s
6b$^{+}_{\text{sym}}$ (D_3) ($^{\text{A/B}}$P-*-F)	0.0738	0.0095	−0.0352	0.0365	164.8	0.594	184.0	10.6	*r*-CS/CT-TBP
6b$^{+}_{\text{nsym}}$ (C_3) ($^{\text{A}}$P–*–F)	0.0212	0.0116	0.0023	0.0118	78.9	1.017	91.6	56.9	*p*-CS/*t*-HB$_{\text{nc}}$
($^{\text{B}}$P-*-F)	0.1843	0.1406	−0.1248	0.1880	131.6	0.149	105.3	0.3	*r*-CS/*t*-HB$_{\text{wc}}$
6c$^{+}_{\text{sym}}$ (C_1) ($^{\text{A/B}}$P-*-Cl)	0.0895	−0.0016	−0.0488	0.0488	181.8	0.331	192.8	0.1	SS/Cov-w
6c$^{+}_{\text{nsym}}$ (C_1) ($^{\text{A}}$P–*–Cl)	0.0433	0.0123	−0.0074	0.0144	120.8	0.623	170.1	56.4	*r*-CS/CT-MC
($^{\text{B}}$P-*-Cl)	0.1670	0.0120	−0.1657	0.1661	175.9	0.201	121.4	3.4	*r*-CS/*t*-HB$_{\text{wc}}$
6d$^{+}_{\text{sym}}$ (C_3) ($^{\text{A/B}}$P-*-Br)	0.0899	−0.0014	−0.0445	0.0445	181.8	0.326	193.8	1.9	SS/Cov-w
6d$^{+}_{\text{nsym}}$ (C_3) ($^{\text{A}}$P–*–Br)	0.0498	0.0112	−0.0109	0.0157	134.3	0.590	181.3	32.2	*r*-CS/CT-TBP
($^{\text{B}}$P-*-Br)	0.1572	−0.0297	−0.1594	0.1621	190.6	0.259	155.2	20.3	SS/Cov-s
6e$^{+}_{\text{sym}}$ (D_3) ($^{\text{A/B}}$P-*-I)	0.0851	−0.0014	−0.0397	0.0397	182.1	0.586	196.9	1.0	SS/Cov-w
7a$^{+}_{\text{nsym}}$ (C_1) ($^{\text{A}}$As–*–H)	0.0222	0.0054	−0.0014	0.0056	104.8	3.013	153.3	199.5	*r*-CS/CT-MC
($^{\text{B}}$As-*-H)	0.1717	−0.0211	−0.1337	0.1354	189.0	0.301	168.3	2.9	SS/Cov-w
7b$^{+}_{\text{sym}}$ (D_3) ($^{\text{A/B}}$As-*-F)	0.0689	0.0226	−0.0186	0.0293	129.4	0.622	133.6	17.3	*r*-CS/*t*-HB$_{\text{wc}}$
7b$^{+}_{\text{nsym}}$ (C_3) ($^{\text{A}}$As–*–F)	0.0200	0.0104	0.0020	0.0106	79.2	1.190	91.0	69.7	*p*-CS/*t*-HB$_{\text{nc}}$
($^{\text{B}}$As-*-F)	0.1734	0.0999	−0.1094	0.1481	137.6	0.174	130.0	1.3	*r*-CS/*t*-HB$_{\text{wc}}$
7c$^{+}_{\text{sym}}$ (C_2) ($^{\text{A/B}}$As-*-Cl)	0.0757	0.0083	−0.0301	0.0312	164.6	0.362	168.4	11.2	*r*-CS/CT-MC
7c$^{+}_{\text{nsym}}$ (C_1) ($^{\text{A}}$As–*–Cl)	0.0394	0.0113	−0.0061	0.0129	118.3	0.712	166.0	57.7	*r*-CS/CT-MC
($^{\text{B}}$As-*-Cl)	0.1471	0.0113	−0.0972	0.0979	173.4	0.245	157.5	2.7	*r*-CS/CT-MC
7d$^{+}_{\text{sym}}$ (C_2) ($^{\text{A/B}}$As-*-Br)	0.0754	0.0057	−0.0296	0.0302	169.2	0.358	176.5	6.9	*r*-CS/CT-MC
7d$^{+}_{\text{nsym}}$ (C_3) ($^{\text{A}}$As–*–Br)	0.0464	0.0101	−0.0098	0.0140	134.2	0.743	198.7	46.2	*r*-CS/CT-TBP
($^{\text{B}}$As-*-Br)	0.1256	−0.0038	−0.0759	0.0760	182.9	0.504	178.4	14.9	SS/Cov-w
8a$^{+}_{\text{sym}}$ (C_3) ($^{\text{A/B}}$Sb-*-H)	0.0689	0.0017	−0.0267	0.0267	176.3	1.108	164.5	25.4	*r*-CS/CT-MC
8a$^{+}_{\text{nsym}}$ (C_1) ($^{\text{A}}$Sb–*–H)	0.0220	0.0047	−0.0019	0.0051	111.8	2.545	162.3	136.5	*r*-CS/CT-MC
($^{\text{B}}$Sb-*-H)	0.1320	0.0098	−0.0754	0.0760	172.6	0.357	153.0	1.4	*r*-CS/CT-MC
8b$^{+}_{\text{sym}}$ (C_3) ($^{\text{A/B}}$Sb-*-F)	0.0632	0.0345	−0.0072	0.0353	101.8	0.596	99.8	5.0	*r*-CS/*t*-HB$_{\text{wc}}$
8b$^{+}_{\text{nsym}}$ (C_3) ($^{\text{A}}$Sb–*–F)	0.0208	0.0096	0.0010	0.0096	84.3	1.821	102.6	66.6	*p*-CS/*t*-HB$_{\text{nc}}$
($^{\text{B}}$Sb-*-F)	0.1353	0.1004	−0.0465	0.1106	114.8	0.200	121.6	1.5	*r*-CS/*t*-HB$_{\text{wc}}$
8c$^{+}_{\text{sym}}$ (D_3) ($^{\text{A/B}}$Sb-*-Cl)	0.0640	0.0162	−0.0183	0.0244	138.5	0.418	124.0	7.8	*r*-CS/*t*-HB$_{\text{wc}}$

Table 2 (*Contd.*)

$\boldsymbol{mx}^{+}_{\text{sym/nsym (symmetry)}}$ ($^{A/B}$Pn-*-X)	$\rho_b(\boldsymbol{r}_c)$ (ea_o^{-3})	$c\nabla^2\rho_b(\boldsymbol{r}_c)^c$ (au)	$H_b(\boldsymbol{r}_c)$ (au)	R^d (au)	θ^e (°)	$C_{ii}{}^f$ (Å mdyn^{-1})	$\theta_p{}^g$ (°)	$\kappa_p{}^h$ (au^{-1})	Predicted nature
8c$^+_{\text{nsym}}$ (C_3) (^{A}Sb–*–Cl)	0.0336	0.0094	−0.0051	0.0107	118.7	0.908	154.0	4.6	*r*-CS/CT-MC
(^{B}Sb-*-Cl)	0.1130	0.0314	−0.0488	0.0580	147.3	0.272	134.6	2.0	*r*-CS/*t*-HB$_{\text{wc}}$

[a] See Table 1 for BSS-B. [b] Data are given at the BCPs. [c] $c\nabla^2\rho_b(\boldsymbol{r}_c) = H_b(\boldsymbol{r}_c) - V_b(\boldsymbol{r}_c)/2$, where $c = \hbar^2/8m$. [d] $R = (x^2 + y^2)^{1/2}$, where $(x, y) = (H_b(\boldsymbol{r}_c) - V_b(\boldsymbol{r}_c)/2, H_b(\boldsymbol{r}_c))$. [e] $\theta = 90° - \tan^{-1}(y/x)$. [f] $C_{ij} = \partial^2E/\partial f_i\partial f_j$, where *i* and *j* refer to internal coordinates, and f_i and f_j, corresponding to *i* and *j*, respectively, are the external force components acting on the system. [g] $\theta_p = 90° - \tan^{-1}(dy/dx)$. [h] $\kappa_p = |d^2y/dx^2|/[1 + (dy/dx)^2]^{3/2}$. [i] Two sets of very close data are predicted from ^{A}Sb-*-H and ^{B}Sb-*-H. One set of data are shown here. [j] Data from $w = \pm0.05$, ±0.025 and 0 are used for the plot because a poor correlation is obtained for the data from $w = \pm0.1$, ±0.05 and 0.0.

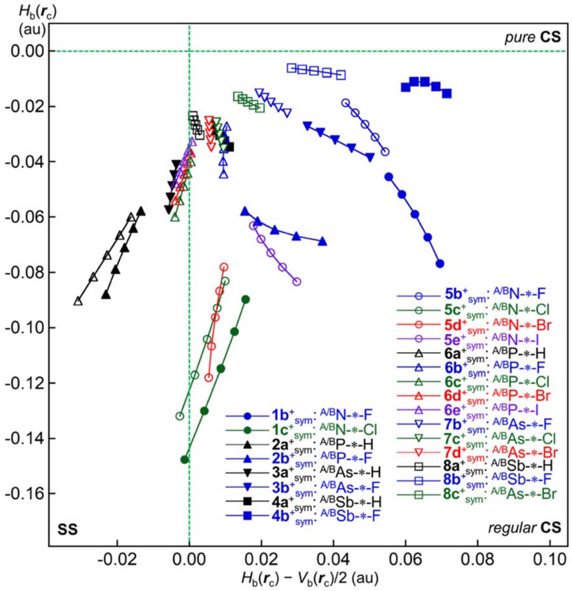

Fig. 5 QTAIM-DFA plots of $^{A/B}$Pn-*-X in $\boldsymbol{mx}^+_{\text{sym}}$ for **1b**$^+$, **1c**$^+$, **2a**$^+$, **2b**$^+$, **3a**$^+$, **3b**$^+$, **4a**$^+$, **4b**$^+$, **5b**$^+$–**5e**$^+$, **6a**$^+$–**6e**$^+$, **7b**$^+$–**7d**$^+$ and **8a**$^+$–**8c**$^+$. See Table 2 for the values of $H_b(\boldsymbol{r}_c)$ and $H_b(\boldsymbol{r}_c) - V_b(\boldsymbol{r}_c)/2$.

While the negative $\nabla^2\rho_b(\boldsymbol{r}_c)$ values ($= 8m/\hbar^2(H_b(\boldsymbol{r}_c) - V_b(\boldsymbol{r}_c)/2)$) were predicted for some interactions, irrespective of the negative Δr_{Cov}($^{A/B}$Pn–X) values, which were examined in more detail through the negative Laplacian maps. Fig. 6 shows the maps for **5a**$^+_{\text{tp:TS}}$, **5a**$^+_{\text{nsym}}$, **6b**$^+_{\text{nsym}}$, **6c**$^+_{\text{nsym}}$, **7b**$^+_{\text{nsym}}$ and **8a**$^+_{\text{nsym}}$, where the maps for **5a**$^+_{\text{tp:TS}}$ and **5a**$^+_{\text{nsym}}$ were very close to those previously reported.[62] Similar maps for those other than those above are shown in Fig. S8 and S9 of the ESI.† The negative $\nabla^2\rho(\boldsymbol{r})$ area near the electronegative atoms around the ^{B}Pn–X interactions was more widely extended relative to that near the electropositive atoms for **2b**$^+_{\text{nsym}}$, **3b**$^+_{\text{nsym}}$, **4a**$^+_{\text{nsym}}$, **6b**$^+_{\text{nsym}}$, **6c**$^+_{\text{nsym}}$, **7b**$^+_{\text{nsym}}$, **7c**$^+_{\text{nsym}}$, **8a**$^+_{\text{nsym}}$, **8b**$^+_{\text{nsym}}$ and **8c**$^+_{\text{nsym}}$, along with $^{A/B}$Pn–X one in **4b**$^+_{\text{sym}}$.

Cremer and Kraka reported that the homonuclear covalent bonds resided in the negative $\nabla^2\rho_b(\boldsymbol{r}_c)$ area, except for F_2, whereas the positive $\nabla^2\rho_b(\boldsymbol{r}_c)$ values sometimes appeared around the heteronuclear bonds.[63] They also demonstrated that distances from the hydrogen atoms to the BCPs changed depending on the differences in the electronegativities of the interacting atoms. As a result, the BCPs moved towards the electropositive atoms rather than the electronegative ones since the electronegative atoms were more negatively charged than the electropositive ones. Similar conditions were observed for ^{B}P-*-F (**2b**$^+_{\text{nsym}}$ and **6b**$^+_{\text{nsym}}$), ^{B}As-*-F (**3b**$^+_{\text{nsym}}$ and **7b**$^+_{\text{nsym}}$), ^{B}Sb-*-H (**4a**$^+_{\text{nsym}}$ and **8a**$^+_{\text{nsym}}$), $^{A/B}$Sb-*-F (**4b**$^+_{\text{sym}}$), ^{B}P-*-Cl (**6c**$^+_{\text{nsym}}$), ^{B}As-*-Cl (**7c**$^+_{\text{nsym}}$), ^{B}Sb-*-F (**8b**$^+_{\text{nsym}}$) and ^{B}Sb-*-Cl (**8c**$^+_{\text{nsym}}$).

$H_b(\boldsymbol{r}_c)$ is a better indicator than $\nabla^2\rho_b(\boldsymbol{r}_c)$ to elucidate the nature of the CS interactions.[63] The $H_b(\boldsymbol{r}_c)$ values for all Pn⋯X⋯Pn bonds in question collected in Table 2 are arranged increasing order, which is shown in eqn (S1) of ESI.† Eqn (4)–(6) show the partial

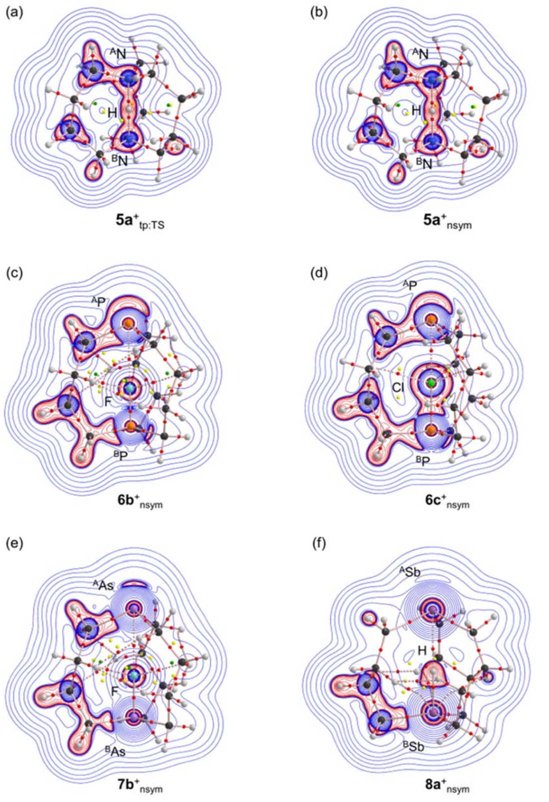

Fig. 6 Negative Laplacian maps of **5a**$^+_{\text{tp:TS}}$, **5a**$^+_{\text{nsym}}$, **6b**$^+_{\text{nsym}}$, **6c**$^+_{\text{nsym}}$, **7b**$^+_{\text{nsym}}$ and **8a**$^+_{\text{nsym}}$ ((a)–(f), respectively), evaluated with MP2/BSS-B. The BCPs are denoted by red dots, RCPs (ring critical points) by yellow dots, CCPs (cage critical points) by green dots and BPs by pink lines. Carbon, hydrogen, phosphorus, arsenic, antimony, fluorine and chlorine atoms are shown in black, grey, orange, light purple, purple, light green and green, respectively. Contour plots are drawn on the planes containing at least ^{A}Pn, ^{B}Pn and X. The red and blue lines correspond to the negative and positive areas of $\nabla^2\rho(\boldsymbol{r})$, respectively.

orders from eqn (S1) of ESI† for X = H, X = F, and X = Cl, Br and I, respectively. Eqn (4) shows that (1) $H_\mathrm{b}(\boldsymbol{r}_\mathrm{c})$ for Pn-*-H increases in the order of $^{\mathrm{B}}$Pn-*-H ($\boldsymbol{ma}^{+}_{\mathrm{nsym}}$) < $^{\mathrm{A/B}}$Pn-*-H ($\boldsymbol{ma}^{+}_{\mathrm{sym}}$) < $^{\mathrm{A}}$Pn–*–H ($\boldsymbol{ma}^{+}_{\mathrm{nsym}}$); (2) regarding $\boldsymbol{m}$, $H_\mathrm{b}(\boldsymbol{r}_\mathrm{c})$ increases in the order of $\boldsymbol{m}$ = (**1** and **5**: Pn = N) < (**2** and **6**: Pn = P) < (**3** and **7**: Pn = As) < (**4** and **8**: Pn = Sb); (3) the order in (2) is clearly observed for the strong interactions in $^{\mathrm{B}}$Pn-*-H and $^{\mathrm{A/B}}$Pn-*-H whereas the order becomes vague for the weak $^{\mathrm{A}}$Pn–*–H. In the case of eqn (5), the trends for X = F are very close to that observed X = H in eqn (4), although some discrepancies are observed in the order, such as $^{\mathrm{A}}$N–*–F ($\mathbf{1b}^{+}_{\mathrm{nsym}}$: −0.016 and $\mathbf{5b}^{+}_{\mathrm{nsym}}$: −0.0015) and $^{\mathrm{A/B}}$P-*-F ($\mathbf{2b}^{+}_{\mathrm{sym}}$: −0.065 and $\mathbf{6b}^{+}_{\mathrm{sym}}$: −0.035). The order in eqn (6) implies that (1) $H_\mathrm{b}(\boldsymbol{r}_\mathrm{c})$ of Pn-*-X increases in the order of X = Cl < Br < I; (2) the same order for $H_\mathrm{b}(\boldsymbol{r}_\mathrm{c})$ of $^{\mathrm{B}}$Pn-*-X ($\boldsymbol{mx}^{+}_{\mathrm{nsym}}$) < $^{\mathrm{A/B}}$Pn-*-X ($\boldsymbol{mx}^{+}_{\mathrm{sym}}$) < $^{\mathrm{A}}$Pn–*–X ($\boldsymbol{mx}^{+}_{\mathrm{nsym}}$) was also observed for X = Cl, Br, and I. However, the order becomes unclear between $^{\mathrm{B}}$Pn-*-X ($\boldsymbol{mx}^{+}_{\mathrm{nsym}}$) and $^{\mathrm{A/B}}$Pn-*-X ($\boldsymbol{mx}^{+}_{\mathrm{sym}}$); (3) the difference in the reactivity between the bicyclo [4.4.4] system *versus* the bicyclo[3.3.3] system becomes much larger for X = Cl, Br, and I, if compared with the case of X = H and F.

Order of $H_\mathrm{b}(\boldsymbol{r}_\mathrm{c})$ for Pn-*-X (X = H):

$^{\mathrm{B}}$N-*-H ($\mathbf{1a}^{+}_{\mathrm{nsym}}$: $H_\mathrm{b}(\boldsymbol{r}_\mathrm{c})$/au = −0.296) < $^{\mathrm{B}}$N-*-H ($\mathbf{5a}^{+}_{\mathrm{nsym}}$: −0.252) < $^{\mathrm{B}}$P-*-H ($\mathbf{2a}^{+}_{\mathrm{nsym}}$: −0.221) < $^{\mathrm{B}}$P-*-H ($\mathbf{6a}^{+}_{\mathrm{nsym}}$: −0.204) < $^{\mathrm{A}}$N–*–H ($\mathbf{1a}^{+}_{\mathrm{nsym}}$: −0.181) < $^{\mathrm{B}}$As-*-H ($\mathbf{3a}^{+}_{\mathrm{nsym}}$: −0.146) < $^{\mathrm{B}}$As-*-H ($\mathbf{7a}^{+}_{\mathrm{nsym}}$: −0.134) < $^{\mathrm{A}}$N–*–H ($\mathbf{5a}^{+}_{\mathrm{nsym}}$: −0.129) < $^{\mathrm{B}}$Sb-*-H ($\mathbf{8a}^{+}_{\mathrm{nsym}}$: −0.075) ≤ $^{\mathrm{B}}$Sb-*-H ($\mathbf{4a}^{+}_{\mathrm{nsym}}$: −0.0744) ≤ $^{\mathrm{A/B}}$P-*-H ($\mathbf{6a}^{+}_{\mathrm{sym}}$: −0.0736) < $^{\mathrm{A/B}}$P-*-H ($\mathbf{2a}^{+}_{\mathrm{sym}}$: −0.071) < $^{\mathrm{A/B}}$As–*–H ($\mathbf{3a}^{+}_{\mathrm{sym}}$: −0.049) < $^{\mathrm{A/B}}$Sb-*-H ($\mathbf{4a}^{+}_{\mathrm{sym}}$: −0.030) < $^{\mathrm{A/B}}$Sb-*-H ($\mathbf{8a}^{+}_{\mathrm{sym}}$: −0.027) < $^{\mathrm{A}}$P–*–H ($\mathbf{2a}^{+}_{\mathrm{nsym}}$: −0.0108) ≤ $^{\mathrm{A}}$As–*–H ($\mathbf{3a}^{+}_{\mathrm{nsym}}$: −0.0101) < $^{\mathrm{A}}$Sb–*–H ($\mathbf{4a}^{+}_{\mathrm{nsym}}$: −0.0097) < $^{\mathrm{A}}$Sb–*–H ($\mathbf{8a}^{+}_{\mathrm{nsym}}$: −0.0019) ≤ $^{\mathrm{A}}$As–*–H ($\mathbf{7a}^{+}_{\mathrm{nsym}}$: −0.0014) ≤ $^{\mathrm{A}}$P–*–H ($\mathbf{6a}^{+}_{\mathrm{nsym}}$: −0.0003) (4)

Order of $H_\mathrm{b}(\boldsymbol{r}_\mathrm{c})$ for Pn-*-X (X = F):

$^{\mathrm{B}}$N-*-F ($\mathbf{1b}^{+}_{\mathrm{nsym}}$: $H_\mathrm{b}(\boldsymbol{r}_\mathrm{c})$/au = −0.332) < $^{\mathrm{B}}$N-*-F ($\mathbf{5b}^{+}_{\mathrm{nsym}}$: −0.283) < $^{\mathrm{B}}$P-*-F ($\mathbf{2b}^{+}_{\mathrm{nsym}}$: −0.134) < $^{\mathrm{B}}$P-*-F ($\mathbf{6b}^{+}_{\mathrm{nsym}}$: −0.125) < $^{\mathrm{B}}$As-*-F ($\mathbf{3b}^{+}_{\mathrm{nsym}}$: −0.120) < $^{\mathrm{B}}$As-*-F ($\mathbf{7b}^{+}_{\mathrm{nsym}}$: −0.109) < $^{\mathrm{A/B}}$P-*-F ($\mathbf{2b}^{+}_{\mathrm{sym}}$: −0.065) < $^{\mathrm{A/B}}$N-*-F ($\mathbf{1b}^{+}_{\mathrm{sym}}$: −0.059) < $^{\mathrm{B}}$Sb-*-F ($\mathbf{8b}^{+}_{\mathrm{nsym}}$: −0.047) < $^{\mathrm{A/B}}$P-*-F ($\mathbf{6b}^{+}_{\mathrm{sym}}$: −0.035) < $^{\mathrm{A/B}}$As-*-F ($\mathbf{3b}^{+}_{\mathrm{sym}}$: −0.032) < $^{\mathrm{A/B}}$N-*-F ($\mathbf{5b}^{+}_{\mathrm{sym}}$: −0.0264) < $^{\mathrm{A/B}}$As-*-F ($\mathbf{7b}^{+}_{\mathrm{sym}}$: −0.019) < $^{\mathrm{A}}$N–*–F ($\mathbf{1b}^{+}_{\mathrm{nsym}}$: −0.016) < $^{\mathrm{A/B}}$Sb-*-F ($\mathbf{4b}^{+}_{\mathrm{sym}}$: −0.0111) < $^{\mathrm{A/B}}$Sb-*-F ($\mathbf{8b}^{+}_{\mathrm{sym}}$: −0.0072) < $^{\mathrm{A}}$P–*–F ($\mathbf{2b}^{+}_{\mathrm{nsym}}$: −0.0039) ≤ $^{\mathrm{A}}$As–*–F ($\mathbf{3b}^{+}_{\mathrm{nsym}}$: −0.0036)) < $^{\mathrm{A}}$N–*–F ($\mathbf{5b}^{+}_{\mathrm{nsym}}$: −0.0015) ≤ $^{\mathrm{A}}$Sb–*–F ($\mathbf{8b}^{+}_{\mathrm{nsym}}$: 0.0010) ≤ $^{\mathrm{A}}$As–*–F ($\mathbf{7b}^{+}_{\mathrm{nsym}}$: 0.0020) ≤ $^{\mathrm{A}}$P–*–F ($\mathbf{6b}^{+}_{\mathrm{nsym}}$: 0.0023) (5)

Order of $H_\mathrm{b}(\boldsymbol{r}_\mathrm{c})$ for Pn-*-X (X = Cl, Br, and I):

$^{\mathrm{B}}$P-*-Cl ($\mathbf{6c}^{+}_{\mathrm{nsym}}$: $H_\mathrm{b}(\boldsymbol{r}_\mathrm{c})$/au = −0166) < $^{\mathrm{B}}$P-*-Br ($\mathbf{6d}^{+}_{\mathrm{nsym}}$: −0.159) > $^{\mathrm{A/B}}$N-*-Cl ($\mathbf{1c}^{+}_{\mathrm{sym}}$: −0.115) < $^{\mathrm{A/B}}$N-*-Cl ($\mathbf{5c}^{+}_{\mathrm{sym}}$: −0.104) < $^{\mathrm{B}}$As-*-Cl ($7\mathrm{c}^{+}_{\mathrm{nsym}}$: −0.097) ≤ $^{\mathrm{A/B}}$N-*-Br ($\mathbf{5d}^{+}_{\mathrm{sym}}$: −0.096) < $^{\mathrm{B}}$As-*-Br ($\mathbf{7d}^{+}_{\mathrm{nsym}}$: −0.076) < $^{\mathrm{A/B}}$N-*-I ($\mathbf{5e}^{+}_{\mathrm{sym}}$: −0.0729) < $^{\mathrm{A/B}}$P-*-Cl ($\mathbf{6c}^{+}_{\mathrm{sym}}$: −0.04881) ≤ $^{\mathrm{B}}$Sb-*-Cl ($\mathbf{8c}^{+}_{\mathrm{nsym}}$: −0.04880) < $^{\mathrm{A/B}}$P-*-Br ($\mathbf{6d}^{+}_{\mathrm{sym}}$: −0.045) < $^{\mathrm{A/B}}$P-*-I ($\mathbf{6e}^{+}_{\mathrm{sym}}$: −0.040) < $^{\mathrm{A/B}}$As-*-Cl ($\mathbf{7c}^{+}_{\mathrm{sym}}$: −0.0301) ≤ $^{\mathrm{A/B}}$As-*-Br ($\mathbf{7d}^{+}_{\mathrm{sym}}$: −0.0296) < $^{\mathrm{A/B}}$Sb-*-Cl ($\mathbf{8c}^{+}_{\mathrm{sym}}$: −0.018) < $^{\mathrm{A}}$P–*–Br ($\mathbf{6d}^{+}_{\mathrm{nsym}}$: −0.0109) ≤ $^{\mathrm{A}}$As–*–Br ($\mathbf{7d}^{+}_{\mathrm{nsym}}$: −0.0098) < $^{\mathrm{A}}$P–*–Cl ($\mathbf{6c}^{+}_{\mathrm{nsym}}$: −0.0074) ≤ $^{\mathrm{A}}$As–*–Cl ($\mathbf{7c}^{+}_{\mathrm{nsym}}$: −0.0061) ≤ $^{\mathrm{A}}$Sb–*–Cl ($\mathbf{8c}^{+}_{\mathrm{nsym}}$: −0.0051) (6)

The strengths of interactions become weakened inversely proportional to $H_\mathrm{b}(\boldsymbol{r}_\mathrm{c})$ being increased. Therefore, the orders in eqn (4) and (5) show the rough orders of the strengths of the interactions being weakened. However, some deviations were observed.

What is the behaviour of $H_\mathrm{b}(\boldsymbol{r}_\mathrm{c})$ in $\mathbf{1a}^{+}$–$\mathbf{8c}^{+}$? Fig. 7 shows the plot of $H_\mathrm{b}(\boldsymbol{r}_\mathrm{c})$ *versus* $\rho_\mathrm{b}(\boldsymbol{r}_\mathrm{c})$ for the sym and nsym shapes of $\mathbf{1a}^{+}$–$\mathbf{8c}^{+}$ (see Table 2 for the data). The plot was analysed, assuming the linear correlations, by the four groups of Group A (G(**A**)), G(**B**), G(**C**) and G(**D**). The correlations are very good for G(**A**) ($y = 0.090–1.57x$: $R_\mathrm{c}^2 = 0.992$), G(**B**) ($y = 0.099–1.35x$: $R_\mathrm{c}^2 = 0.987$) and G(**C**) ($y = 0.136–1.38x$: $R_\mathrm{c}^2 = 0.994$) and fairly good for G(**D**) ($y = 0.007–0.35x$: $R_\mathrm{c}^2 = 0.78$). The plot for G(**A**) appears most downside of the four and that for G(**C**) does most upside, while that for G(**B**) exists between the two. The data for G(**D**) correspond to those from the much weaker bonds of $^{\mathrm{A}}$Pn–*–X in the nsym shapes; therefore, the (data) points are located near the origin of the plots. The correlation constant for G(**D**) is about one-fourth to one-fifth of those for G(**A**), G(**B**) and G(**C**). Most of the data are contained in G(**A**), which consists of the data from 14 sym shapes and seven nsym shapes. G(**B**) contains those from five sym shapes and eight nsym shapes. While G(**C**) contains four sym shapes seven nsym shapes G(**D**) does those for 16 nsym shapes, except for four (see Fig. 7 for the interactions and the species).

The trend in the correlations can be variously explained, but our explanation is as follows: Almost common mechanisms are operating to give $H_\mathrm{b}(\boldsymbol{r}_\mathrm{c})$ and $\rho_\mathrm{b}(\boldsymbol{r}_\mathrm{c})$ for both sym and nsym shapes of $\mathbf{1a}^{+}$–$\mathbf{8c}^{+}$. The mechanisms to give $H_\mathrm{b}(\boldsymbol{r}_\mathrm{c})$ and/or $\rho_\mathrm{b}(\boldsymbol{r}_\mathrm{c})$ would be very similar for most species but somewhat different for some

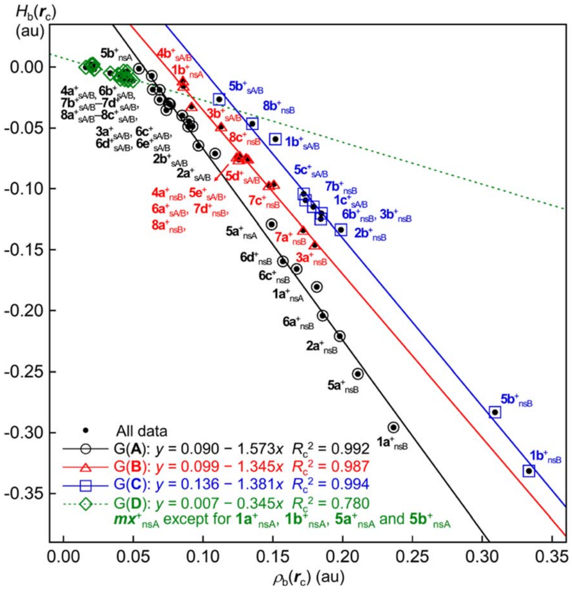

Fig. 7 Plots of $H_\mathrm{b}(\boldsymbol{r}_\mathrm{c})$ *versus* $\rho_\mathrm{b}(\boldsymbol{r}_\mathrm{c})$ for Pn-*-X in $\mathbf{1a}^{+}$–$\mathbf{8c}^{+}$, evaluated with MP2/BSS-B.

species. The species with the negligibly small differences in the mechanisms forms a group of G(**A**), G(**B**), G(**C**) or G(**D**); however, there are some differences among the groups.

The natures of the secondary interactions of X–*–C and H–*–H for **1–8** and **1a**$^+$–**8c**$^+$ were also investigated with MP2/BSS-B, along with $^{\rm A}$Pn–*–$^{\rm B}$Pn of **1**, **5** and **6**. The QTAIM functions and QTAIM-DFA parameters are provided in Table S6 of the ESI,† along with the C_{ii} values, corresponding to generate the perturbed structures, and the predicted natures. Various natures of *p*-CS/vdW, *p*-CS/*t*-HB$_{\rm nc}$, *r*-CS/*t*-HB$_{\rm wc}$ and *r*-CS/CT-MC were predicted for X–*–C and H–*–H, together with $^{\rm A}$Pn–*–$^{\rm B}$Pn. These interactions contributed to stabilizing the system, in addition to $^{\rm A/B}$Pn-*-X, $^{\rm A}$Pn–*–X and $^{\rm B}$Pn-*-X.

The natures were also elucidated for the interactions in question in the transition states. The analysed results by QTAIM-DFA are collected in Table S7 of the ESI,† along with molecular graphs and negative Laplacian maps shown in Fig. S10 and S11 of the ESI,† respectively.

Second-perturbation energies *E*(2)

The contributions from the CT terms of NBO(*i*) → NBO(*j*) to **1a**$^+$–**8c**$^+$ were estimated through the second-perturbation energies (*E*(2)), calculated using the NBO analysis with M06-2X/BSS-B//MP2/BSS-B. Table 3 lists the *E*(2) values for **1a**$^+$–**8c**$^+$. Several types of the CT terms contribute to stabilize the species. The first is the n($^{\rm A}$Pn) → σ*(X–$^{\rm B}$Pn) type, which operates in 17 species. The *E*(2) values are shown in parenthesis after the compound: The values larger than 30 kcal mol^{-1} are **1a**$^+_{\rm nsym}$ (*E*(2) = 78 kcal mol^{-1}), **5a**$^+_{\rm nsym}$ (80 kcal mol^{-1}), **1b**$^+_{\rm sym}$ (344 kcal mol^{-1}), **1c**$^+_{\rm sym}$ (230 kcal mol^{-1}), **2b**$^+_{\rm sym}$ (565 kcal mol^{-1}), **5b**$^+_{\rm sym}$ (243 kcal mol^{-1}), **5c**$^+_{\rm sym}$ (191 kcal mol^{-1}), **5d**$^+_{\rm sym}$ (171 kcal mol^{-1}), **5e**$^+_{\rm sym}$ (132 kcal mol^{-1}), **6a**$^+_{\rm sym}$ (288 kcal mol^{-1}), **6c**$^+_{\rm sym}$ (357 kcal mol^{-1}), **7c**$^+_{\rm sym}$ (506 kcal mol^{-1}), **8a**$^+_{\rm sym}$ (349 kcal mol^{-1}), **8b**$^+_{\rm sym}$ (429 kcal mol^{-1}), and **8c**$^+_{\rm sym}$ (762 kcal mol^{-1}). The *E*(2) values for the nsym shapes are small to moderate, whereas the values are very large for the sym shapes. The shorter interaction distances in the sym shapes would be responsible for the results.

The second is the σ($^{\rm A}$Pn–C/$^{\rm B}$Pn–C) → n$_{\rm p}$(X$^+$) type, which operates in 6 species of **2a**$^+_{\rm sym}$ (335 kcal mol^{-1}), **3a**$^+_{\rm sym}$ (448 kcal mol^{-1}), **4a**$^+_{\rm sym}$ (566 kcal mol^{-1}), **6d**$^+_{\rm sym}$ (369 kcal mol^{-1}), **6e**$^+_{\rm sym}$ (353 kcal mol^{-1}) and **7d**$^+_{\rm sym}$ (460 kcal mol^{-1}). Total six equivalent σ(Pn–C) bonds from three σ($^{\rm A}$Pn–C) and three σ($^{\rm B}$Pn–C) bonds contribute to this type; therefore, the total contribution is six times larger than that of each contribution. The total values are also very large. The third case is the σ($^{\rm A}$Pn–C) → σ*(X–$^{\rm B}$Pn) form, which operates in 14 species. The total contribution is three times larger than that of each contribution. The total contributions larger than 30 kcal mol^{-1} are **3a**$^+_{\rm nsym}$ (41 kcal mol^{-1}), **4a**$^+_{\rm nsym}$ (43 kcal mol^{-1}). The fourth is the n$_{\rm p}$(F) → σ*($^{\rm A}$Pn–$^{\rm B}$Pn), which operated in **6b**$^+_{\rm sym}$ (102 kcal mol^{-1}) and **7b**$^+_{\rm sym}$ (80 kcal mol^{-1}). Other cases of which contributions larger than 10 kcal mol^{-1} are n($^{\rm A}$P/$^{\rm B}$P) → σ(H$^+$) (32 kcal mol^{-1}) in **2a**$^+_{\rm sym}$ and n(F) → n(Sb$^+$) (67 kcal mol^{-1}) in **4b**$^+_{\rm sym}$.

The high contributions from the CT terms mainly arise from the n($^{\rm A}$Pn) → σ*(X–$^{\rm B}$Pn) types. The σ($^{\rm A}$Pn–C/$^{\rm B}$Pn–C) → n$_{\rm p}$(X$^+$) type interactions also have the substantially high contributions. The reason for the contributions was intriguing at first glance but it would be difficult to explain. The reason could be interpreted by considering the through space and the through bond mechanisms. The contributions increased rapidly as the interaction distances became shorter. The contributions in question could be understood based on the same reason. A similar mechanism would also operate in the CT interactions in σ($^{\rm A}$Pn–C/$^{\rm B}$Pn–C) → n$_{\rm p}$(X$^+$).

The very high contributions from the of n($^{\rm A}$Pn) → σ*(X–$^{\rm B}$Pn) type, accompanied by the very large *E*(2) values, must correlate deeply to the (very) high p-characters in n($^{\rm A}$Pn). The occupancy ratios between s- and p-characters in n($^{\rm A}$Pn) were calculated under the same conditions. The results are shown in Table S8 of the ESI.† The planarity around $^{\rm A}$Pn will affect much to the ratio of the p-character, together with the energy difference between atomic s- and p-orbitals of $^{\rm A}$Pn. High ratios of p-characters over 70% were predicted for n($^{\rm A}$Pn) in **1a**$^+$–**1c**$^+$ (86.0–98.7%), **2b**$^+$ (97.6%), **3b**$^+$ (97.4%), **5a**$^+$–**5e**$^+$ (84.4–99.6%), **6a**$^+$ (87.9%), **6c**$^+$ (96.2%), **7c**$^+$ (96.5%), **8a**$^+$ (92.6%), **8b**$^+$(97.7%) and **8c**$^+$ (96.3%). However, the predicted rations were 32.1–62.4% for the others. Indeed, high ratios of the p-characters are expected to enlarge *E*(2) for n($^{\rm A}$Pn) → σ*(X–$^{\rm B}$Pn), but the correlation between the ratio and *E*(2) seems unclear, as shown in Table 3. Other factors, such as the atomic types of $^{\rm A}$Pn, X and $^{\rm B}$Pn, must also operate to control the *E*(2) values.

The NBO analysis demonstrated the large contributions from the $^{\rm A}$Pn–X–$^{\rm B}$Pn and $^{\rm A}$Pn⋯X–$^{\rm B}$Pn interactions and clarified the reasons for the high contributions from n($^{\rm A}$Pn) → σ*(X–$^{\rm B}$Pn). While the σ($^{\rm A}$Pn–C/$^{\rm B}$Pn–C) → n$_{\rm p}$(X$^+$) interactions also contribute much to stabilise the system, the contributions from σ($^{\rm A}$Pn–C) → σ*(X–$^{\rm B}$Pn) seem smaller. The contribution from n(F) → n$_{\rm s}$(Sb$^+$) was also of interest. The n(F) → n$_{\rm s}$(Sb$^+$) interaction, in place of n$_{\rm p}$(Sb) → σ*(F–Sb), contributed to **4b**$^+_{\rm sym}$. A heavy CT occurred from Sb to F$^+$ due to the very large electronegativity of F, relative to Sb, resulting in the formation of F and Sb$^+$, which led to the above interaction, as listed in Table 3.

Characteristic nature of [Pn–X–Pn]$^+$ with the behaviour of charge

What is the character of Pn–X$^+$–Pn in **1a**$^+$–**8c**$^+$? The ψ_3, ψ_2 and ψ_1 orbitals of σ(3c–4e) are looked for among MOs in **1a**$^+$–**8c**$^+$. Fig. 8 shows HOMO-5, HOMO and LUMO of **6c**$^+_{\rm sym}$, for example, which correspond to the orbitals, respectively. The results clearly demonstrate the σ(3c–4e) nature for Pn–X$^+$–Pn.

How are the behaviour of Qn, in relation to σ(3c–4e)? The sym and nsym shapes are optimized for all **6a**$^+$–**6e**$^+$, except for **6e**$^+_{\rm sym}$; therefore, it is convenient to discuss the overall trends in the changes of Qn, so are **5**$^+$, **7**$^+$ and **8**$^+$. Fig. 9 shows the plot of Qn($^{\rm A}$P), Qn(X), Qn($^{\rm B}$P) and Qn(Total) (= Qn(T) = Qn($^{\rm A}$P) + Qn(X) + Qn($^{\rm B}$P)) for **6a**$^+_{\rm sym}$–**6e**$^+_{\rm sym}$ and **6a**$^+_{\rm nsym}$–**6d**$^+_{\rm nsym}$ *versus* X. The values of Qn($^{\rm A}$P), Qn(X), Qn($^{\rm B}$P) and Qn(T) for **1–8** and **1a**$^+$–**8c**$^+$ are collected in Table S8 of the ESI.†

Table 3 Contributions from the CT terms of the NBO(i)→NBO(j) form to the interactions in $\mathbf{1a}^{+}$–$\mathbf{8c}^{+}$, estimated through the second-perturbation energies ($E(2)$), evaluated with NBO analysis under the M06-2X/BSS-B//MP2/BSS-B conditions.^{a}

Species ($^{\mathrm{A}}$Pn ($^{\mathrm{B}}$Pn), X)	NBO(i)→NBO(j)	$E(2)^{b}$ (kcal mol^{-1})	$F(i,j)^{c}$ (au)	Species ($^{\mathrm{A}}$Pn ($^{\mathrm{B}}$Pn), X)	NBO(i)→NBO(j)	$E(2)^{b}$ (kcal mol^{-1})	$F(i,j)^{c}$ (au)
$\mathbf{1a}^{+}_{\mathrm{nsym}}$ (N, H)	n($^{\mathrm{A}}$N) → σ*(H–$^{\mathrm{B}}$N)	77.6	0.212	$\mathbf{6a}^{+}_{\mathrm{sym}}$ (P, H)	n($^{\mathrm{A/B}}$P) → σ*(H–$^{\mathrm{B/A}}$P)	288.1^{d}	0.256
$\mathbf{1b}^{+}_{\mathrm{sym}}$ (N, F)	n($^{\mathrm{A/B}}$N) → σ*(F–$^{\mathrm{B/A}}$N)	344.2^{d}	0.198	$\mathbf{6a}^{+}_{\mathrm{nsym}}$ (P, H)	σ($^{\mathrm{A}}$P–C) → σ*(H–$^{\mathrm{B}}$P)	4.2^{g} (12.6)^{f}	0.052
$\mathbf{1b}^{+}_{\mathrm{nsym}}$ (N, F)	n($^{\mathrm{A}}$N) → σ*(F–$^{\mathrm{B}}$N)	11.1	0.064	$\mathbf{6b}^{+}_{\mathrm{sym}}$ (P, F)	n(F) → σ*($^{\mathrm{A}}$P–$^{\mathrm{B}}$P)	101.8	0.171
$\mathbf{1c}^{+}_{\mathrm{sym}}$ (N, Cl)	n($^{\mathrm{A/B}}$N) → σ*(Cl–$^{\mathrm{B/A}}$N)	229.6^{d}	0.277	$\mathbf{6b}^{+}_{\mathrm{nsym}}$ (P, F)	^{h}	^{h}	^{h}
$\mathbf{2a}^{+}_{\mathrm{sym}}$ (P, H)	n($^{\mathrm{A}}$P/$^{\mathrm{B}}$P) → s(H^{+})	31.9	0.060	$\mathbf{6c}^{+}_{\mathrm{sym}}$ (P, Cl)	n($^{\mathrm{A/B}}$P) → σ*(Cl–$^{\mathrm{B/A}}$P)	356.9^{d}	0.171
	σ($^{\mathrm{A}}$P–C/$^{\mathrm{B}}$P–C) → s(H^{+})	55.8^{e} (334.8)^{f}	0.134	$\mathbf{6c}^{+}_{\mathrm{nsym}}$ (P, Cl)	σ($^{\mathrm{A}}$P–C) → σ*(Cl–$^{\mathrm{B}}$P)	1.4^{g} (4.1)^{f}	0.031
$\mathbf{2a}^{+}_{\mathrm{nsym}}$ (P, H)	σ($^{\mathrm{A}}$P–C) → σ*(H–$^{\mathrm{B}}$P)	10.1^{g} (30.3)^{f}	0.083	$\mathbf{6d}^{+}_{\mathrm{sym}}$ (P, Br)	σ($^{\mathrm{A}}$P–C/$^{\mathrm{B}}$P–C) → n(Br^{+})	61.5^{e} (369.2)^{f}	0.116
$\mathbf{2b}^{+}_{\mathrm{sym}}$ (P, F)	n($^{\mathrm{A}}$P) → σ*(F–$^{\mathrm{B}}$P)	565.0	0.142	$\mathbf{6d}^{+}_{\mathrm{nsym}}$ (P, Br)	σ($^{\mathrm{A}}$P–C) → σ*(Br–$^{\mathrm{B}}$P)	8.3^{g} (24.8)^{f}	0.066
$\mathbf{2b}^{+}_{\mathrm{nsym}}$ (P, F)	σ($^{\mathrm{A}}$P–C) → σ*(F–$^{\mathrm{B}}$P)	1.2^{g} (3.6)^{f}	0.027	$\mathbf{6e}^{+}_{\mathrm{sym}}$ (P, I)	σ($^{\mathrm{A}}$P–C/$^{\mathrm{B}}$P–C) → n(I^{+})	58.9^{e} (353.2)^{f}	0.122
$\mathbf{3a}^{+}_{\mathrm{sym}}$ (As, H)	σ($^{\mathrm{A}}$As–C/$^{\mathrm{B}}$As–C) → s(H^{+})	74.6^{e} (447.6)^{f}	0.138	$\mathbf{7a}^{+}_{\mathrm{nsym}}$ (As, H)	σ($^{\mathrm{A}}$As–C) → σ*(H–$^{\mathrm{B}}$As)	7.0^{g} (21.0)^{f}	0.065
$\mathbf{3a}^{+}_{\mathrm{nsym}}$ (As, H)	σ($^{\mathrm{A}}$As–C) → σ*(H–$^{\mathrm{B}}$As)	13.5^{g} (40.5)^{f}	0.091	$\mathbf{7b}^{+}_{\mathrm{sym}}$ (As, F)	n(F) → σ*($^{\mathrm{A}}$As–$^{\mathrm{B}}$As)	80.0	0.147
$\mathbf{3b}^{+}_{\mathrm{sym}}$ (As, F)	σ($^{\mathrm{A}}$As–C) → σ*(F–$^{\mathrm{B}}$As)	3.3^{g} (9.8)^{f}	0.037	$\mathbf{7b}^{+}_{\mathrm{nsym}}$ (As, F)	^{h}	^{h}	^{h}
$\mathbf{3b}^{+}_{\mathrm{nsym}}$ (As, F)	σ($^{\mathrm{A}}$As–C) → σ*(F–$^{\mathrm{B}}$As)	1.2^{g} (3.6)^{f}	0.025	$\mathbf{7c}^{+}_{\mathrm{sym}}$ (As, Cl)	n($^{\mathrm{A/B}}$As) → σ*(Cl–$^{\mathrm{B/A}}$As)	505.8^{d}	0.151
$\mathbf{4a}^{+}_{\mathrm{sym}}$ (Sb, H)	σ($^{\mathrm{A}}$Sb–C/$^{\mathrm{B}}$Sb–C) → s(H^{+})	94.3^{e} (565.7)^{f}	0.123	$\mathbf{7c}^{+}_{\mathrm{nsym}}$ (As, Cl)	σ($^{\mathrm{A}}$As–C) → σ*(Cl–$^{\mathrm{B}}$As)	4.3^{g} (12.8)^{f}	0.046
$\mathbf{4a}^{+}_{\mathrm{nsym}}$ (Sb, H)	σ($^{\mathrm{A}}$Sb–C) → σ*(H–$^{\mathrm{B}}$Sb)	14.3^{g} (43.0)^{f}	0.086	$\mathbf{7d}^{+}_{\mathrm{sym}}$ (As, Br)	σ($^{\mathrm{A}}$As–C/$^{\mathrm{B}}$As–C) → n(Br^{+})	76.6^{e} (459.5)^{f}	0.111
$\mathbf{4b}^{+}_{\mathrm{sym}}$ (Sb, F)	n(F) → n(Sb^{+})	66.8	0.066	$\mathbf{7d}^{+}_{\mathrm{nsym}}$ (As, Br)	σ($^{\mathrm{A}}$As–C) → σ*(Br–$^{\mathrm{B}}$As)	9.9^{g} (29.7)^{f}	0.067
$\mathbf{5a}^{+}_{\mathrm{nsym}}$ (N, H)	n($^{\mathrm{A/B}}$N) → σ*(H–$^{\mathrm{B/A}}$N)	80.4^{d}	0.220	$\mathbf{8a}^{+}_{\mathrm{sym}}$ (Sb, H)	n($^{\mathrm{A/B}}$Sb) → σ*(H–$^{\mathrm{B/A}}$Sb)	348.6^{d}	0.184
$\mathbf{5b}^{+}_{\mathrm{sym}}$ (N, F)	n($^{\mathrm{A/B}}$N) → σ*(F–$^{\mathrm{B/A}}$N)	242.7^{d}	0.162	$\mathbf{8a}^{+}_{\mathrm{nsym}}$ (Sb, H)	σ($^{\mathrm{A}}$Sb–C) → σ*(H–$^{\mathrm{B}}$Sb)	6.7^{g} (20.0)^{f}	0.059
$\mathbf{5b}^{+}_{\mathrm{nsym}}$ (N, F)	n($^{\mathrm{A}}$N) → σ*(F–$^{\mathrm{B}}$N)	12.0	0.058	$\mathbf{8b}^{+}_{\mathrm{sym}}$ (Sb, F)	n($^{\mathrm{A}}$Sb) → σ*(F–$^{\mathrm{B}}$Sb)	429.2	0.086
$\mathbf{5c}^{+}_{\mathrm{sym}}$ (N, Cl)	n($^{\mathrm{A/B}}$N) → σ*(Cl–$^{\mathrm{B/A}}$N)	191.4^{d}	0.259	$\mathbf{8b}^{+}_{\mathrm{nsym}}$ (Sb, F)	n(F) → σ*($^{\mathrm{A}}$Sb–C)	1.7^{g} (5.1)^{f}	0.042
$\mathbf{5d}^{+}_{\mathrm{sym}}$ (N, Br)	n($^{\mathrm{A/B}}$N) → σ*(Br–$^{\mathrm{B/A}}$N)	170.5^{d}	0.251	$\mathbf{8c}^{+}_{\mathrm{sym}}$ (Sb, Cl)	n($^{\mathrm{A/B}}$Sb) → σ*(Cl–$^{\mathrm{B/A}}$Sb)	762.1^{d}	0.130
$\mathbf{5e}^{+}_{\mathrm{sym}}$ (N, I)	n($^{\mathrm{A/B}}$N) → σ*(I–$^{\mathrm{B/A}}$N)	131.8^{d}	0.231	$\mathbf{8c}^{+}_{\mathrm{nsym}}$ (Sb, Cl)	σ($^{\mathrm{A}}$Sb–C) → σ*(H–$^{\mathrm{B}}$Sb)	2.9^{g} (8.6)^{f}	0.035

[a] See Table 1 for BSS-B. [b] Second-perturbation energy. [c] The off-diagonal NBO Fock matrix elements. [d] Detected as σ(3c–4e). [e] Six CT contributions are detected. [f] Total values are given in parenthesis. [g] Three CT contributions are detected. [h] No CT contributions in question are detected.

The Qn(X) values in sym and nsym shapes of $\mathbf{6a}^{+}$–$\mathbf{6e}^{+}$ become larger in the order of X = F < Cl < Br < I, as expected, where Qn(H) seems close to Qn(Cl) or Qn(Br). Qn(P) behaves the exact opposite of Qn(X). The exact opposite behaviour between Qn(P) (or Qn($^{\mathrm{B}}$Pn)) and Qn(X) are confirmed by examining Qn(T), which are almost constant for both shapes. It is noteworthy that Qn($^{\mathrm{A}}$P) are almost constant in the nsym shapes, irrespective of the large changes in Qn(X) and Qn($^{\mathrm{B}}$Pn). The results may support the formation of the (very) strong $^{\mathrm{B}}$P–X bond with the (very) weak $^{\mathrm{A}}$Pn⋯X in the nsym shapes. The plots for $\mathbf{5}^{+}$, $\mathbf{7}^{+}$ and $\mathbf{8}^{+}$, drawn in Fig. S12 of the ESI,† are very similar to that in Fig. 9.

It seems curious that the Qn(T) values of $\mathbf{6a}^{+}_{\mathrm{sym}}$–$\mathbf{6e}^{+}_{\mathrm{sym}}$ are close to 2 (e^{+}), which is much larger than 1 (e^{+}), originated from X^{+}, at first glance. The results could be very different from those generally expected for the formation of σ(3c–4e). Fig. 10 explains the changes of Qn($^{\mathrm{A/B}}$P) and Qn(X) in the formation of $\mathbf{6c}^{+}_{\mathrm{sym}}$, starting from $\mathbf{6}_{\mathrm{nsym}}$ + Cl^{+}, *via* $[\mathbf{6c}^{+}_{\mathrm{nsym}}]_{\mathrm{CT=0}}$. Our explanation for the change in Qn is as follows. The mechanism for the change is explained by the three processes, starting from the neutral $\mathbf{6}_{\mathrm{nsym}}$ + Cl^{+}. (1) The Qn($^{\mathrm{A}}$Pn/$^{\mathrm{B}}$Pn) values in $\mathbf{6}_{\mathrm{nsym}}$ are 0.78e^{+} and 0.82e^{+}, respectively. (2) When Cl^{+} is incorporated into P⋯P of $\mathbf{6}_{\mathrm{nsym}}$, the double donation occurs from the lone pair electrons of P to the vacant p-orbital of Cl^{+}. The Qn(Pn) and Qn(Cl) values would be 1.8e^{+} and −1.0e^{+}, respectively, where the donated electrons are assumed to share equally between P and Cl. The primitive structure with no CT is denoted by

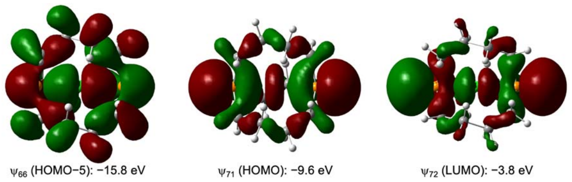

Fig. 8 HOMO−5, HOMO and LUMO in $\mathbf{6c}^{+}_{\mathrm{sym}}$ (Pn = P, X = Cl), which correspond to ψ_1, ψ_2 and ψ_3 of σ(3c–4e), respectively.

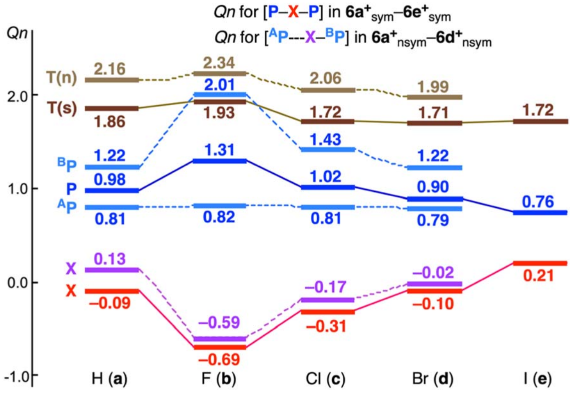

Fig. 9 Plots of Qn($^{\mathrm{A}}$Pn), Qn(X), Qn($^{\mathrm{B}}$Pn) and Qn(T) *versus* X for $\mathbf{6a}^{+}$–$\mathbf{6e}^{+}$.

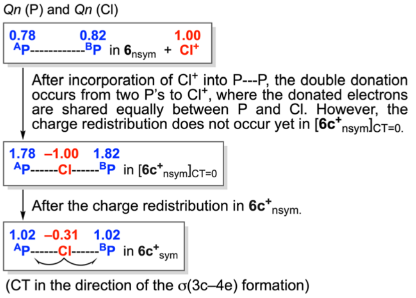

Fig. 10 Changes in Qn($^{A/B}$Pn) and Qn(X) in the formation of **6c**$^{+}_{sym}$ *via* [**6c**$^{+}_{nsym}$]$_{CT=0}$.

[**6c**$^{+}_{nsym}$]$_{CT=0}$. (3) The charges in P–Cl–P of [**6c**$^{+}_{nsym}$]$_{CT=0}$ redistribute to form **6c**$^{+}_{sym}$.

The CT occurs from [**6c**$^{+}_{nsym}$]$_{CT=0}$ to **6c**$^{+}_{sym}$, contrary to the electronegativities of P and Cl, in this process, resulting in Qn(Pn) = 1.02e^{+} and Qn(Cl) = −0.31e^{+}. The σ(3c–4e) character of ^{A}Pn–X^{+}–^{B}Pn is demonstrated again, through the examination of the changes of the charges on the atoms. Indeed, some Pn–X^{+}–Pn interactions would not be typical σ(3c–4e), depending on the combination of Pn and X, but the bonds, analysed in this work, are recognized to be the σ(3c–4e) type, for the unified understanding of the bonds.

The σ-hole on a halogen atom must correlate deeply in the behavior of ^{A}Pn–X^{+}–^{B}Pn and/or Pn⋯X^{+}–Pn. Molecular electrostatic potentials (MEPs) will present a fine picture for the visualization. The MEPs are shown in Fig. S13 of the ESI,† exemplified by **6d**$^{+}_{nsym}$, [H–C(CH$_2$CH$_2$CH$_2$CH$_2$)$_3$P–Br]$^{+}$ (**9d**$^{+}$) and [H–C(CH$_2$CH$_2$CH$_2$CH$_2$)$_3$P–I]$^{+}$ (**9e**$^{+}$).

Conclusions

The possibility of large atoms to incorporate in stable cage compounds of medium rings was examined with the atoms X of H (**a**), F (**b**), Cl (**c**), Br (**d**) and I (**e**). The skeletons of bicyclo[3.3.3]undecane and bicyclo[4.4.4]tetradecane were employed for the purpose, in which the bridgehead atoms were substituted by pnictogens (^{A}Pn = ^{B}Pn = N, P, As and Sb: **1*x***$^{+}$–**8*x***$^{+}$). In this system, X acted as X^{+} to form the linear ^{A}Pn–X^{+}–^{B}Pn σ(3c–4e) type interactions, which were fixed by the bicyclo systems. Moreover, **1**$^{+}$ (^{A}Pn = ^{B}Pn = N) was successfully optimized for X of each H, F and Cl, and **2*x***$^{+}$ (^{A}Pn = ^{B}Pn = P), **3*x***$^{+}$ (^{A}Pn = ^{B}Pn = As) and **4*x***$^{+}$ (^{A}Pn = ^{B}Pn = Sb) were carefully optimized when X = H and F. In the case of **5*x***$^{+}$ (^{A}Pn = ^{B}Pn = N) and **6*x***$^{+}$ (^{A}Pn = ^{B}Pn = P) were successfully optimized for X of H, F, Cl, Br and I, **7*x***$^{+}$ (^{A}Pn = ^{B}Pn = As) was optimized for X of H, F, Cl and Br, and **8*x***$^{+}$ (^{A}Pn = ^{B}Pn = Sb) was optimized for X of H, F and Cl. The structures of the symmetric and nonsymmetric shapes were optimized for **1a**$^{+}$–**8c**$^{+}$, with their relative stabilities, and their transition states. The symmetric shapes appeared to be more stabilized as ^{A}Pn, ^{B}Pn and X became larger, with the exception of ^{A}Pn = ^{B}Pn = N.

The intrinsic dynamic and static natures of the Pn-*-X interactions were elucidated for **1a**$^{+}$–**8c**$^{+}$ with QTAIM-DFA. Various natures from vdW to Cov-s were predicted. The ^{B}P-*-F (**2b**$^{+}_{nsym}$ and **6b**$^{+}_{nsym}$), ^{B}As-*-F (**3b**$^{+}_{nsym}$ and **7b**$^{+}_{nsym}$), ^{B}Sb-*-H (**4a**$^{+}_{nsym}$ and **8a**$^{+}_{nsym}$), $^{A/B}$Sb-*-F (**4b**$^{+}_{sym}$), ^{B}P-*-Cl (**6c**$^{+}_{nsym}$), ^{B}As-*-Cl (**7c**$^{+}_{nsym}$), ^{B}Sb-*-F (**8b**$^{+}_{nsym}$) and ^{B}Sb-*-Cl (**8c**$^{+}_{nsym}$) interactions were predicted to be *r*-CS/*t*-HB$_{wc}$ or *r*-CS/CT-MC, respectively, although their $r(^{A/B}$Pn–X) were shorter than the $r_{Cov}(^{A/B}$Pn–X). In contrast, the SS/Cov-w or SS/Cov-s natures were predicted for ^{B}Pn-*-X interactions than the above such as ^{B}N-*-H in **1a**$^{+}_{nsym}$ and **5a**$^{+}_{nsym}$ (with **1a**$^{+}_{tp:TS}$ and **5a**$^{+}_{tp:TS}$). The secondary interactions of H-*-H and X-*-C were also detected, of which the predicted natures were *p*-CS/vdW, *p*-CS/*t*-HB$_{nc}$, *r*-CS/*t*-HB$_{wc}$ and *r*-CS/CT-MC. They also contributed to stabilising the systems, along with the main interactions. The order of the interaction strengths was estimated using the $H_b(\boldsymbol{r}_c)$ values.

The NBO analysis was applied to the interactions and evaluated the contributions from the CT terms to the interactions in question. Several types of NBO(*i*) to NBO(*j*) interactions were detected in this case. Among the several types, the n$_p$(^{A}Pn)→σ*(X–^{B}Pn) interactions highly contributed, together with σ(^{A}Pn–C)→σ*(X–^{B}Pn) and σ(^{A}Pn–C/^{B}Pn–C)→n$_p$(X^{+}). In the case of **4b**$^{+}$, the CT interaction was described by n$_p$(F)→n$_s$(Sb^{+}), not by n$_p$(Sb)→σ*(F–Sb). The very large electronegativity of F was likely responsible for the change. The charge distributions on the atoms of ^{A}Pn–X^{+}–^{B}Pn were confirmed to show the σ(3c–4e) type behaviour.

Our results provide important insights into the nature of the interactions, especially the hypervalent 3c–4e interactions of the symmetric and nonsymmetric shapes, where the interactions are fixed linearly by the bicyclo systems. These interactions can also be considered as the extension of the hydrogen and halogen bonds. These results are useful to design materials containing X^{+}, as in **1–8**.

Author contributions

S. H. formulated the project. T. N. contributed to conceptualization, investigation and writing – original draft. W. N. and S. H. contributed to supervision, data curation, resources and writing – review & editing. All authors have read and agreed to the published version of the manuscript.

Conflicts of interest

The authors declare no conflicts of interest.

Acknowledgements

The computations were partially performed at the Research Centre for Computational Science, Okazaki, Japan.

Notes and references

1 W. Nakanishi, S. Hayashi and K. Narahara, *J. Phys. Chem. A*, 2009, **113**, 10050–10057.
2 W. Nakanishi and S. Hayashi, *Curr. Org. Chem.*, 2010, **14**, 181–197.
3 W. Nakanishi and S. Hayashi, *J. Phys. Chem. A*, 2010, **114**, 7423–7430.

4 W. Nakanishi, S. Hayashi, K. Matsuiwa and M. Kitamoto, *Bull. Chem. Soc. Jpn.*, 2012, **85**, 1293–1305.
5 S. Hayashi, K. Matsuiwa, M. Kitamoto and W. Nakanishi, *J. Phys. Chem. A*, 2013, **117**, 1804–1816.
6 S. Hayashi, T. Nishide, W. Nakanishi, L. Sancineto and C. Santi, *RSC Adv.*, 2019, **9**, 39435–39446.
7 G. Montà-González, F. Sancenón, R. Martínez-Máñez and V. Martí-Centelles, *Chem. Rev.*, 2022, **122**, 13636–13708.
8 X. Yang, Z. Ullah, J. F. Stoddart and C. T. Yavuz, *Chem. Rev.*, 2023, **123**, 4602–4634.
9 R. W. Alder, *Tetrahedron*, 1990, **46**, 683–713.
10 J. G. Verkade, *Coord. Chem. Rev.*, 1994, **137**, 233–295.
11 R. W. Alder and D. Read, *Coord. Chem. Rev.*, 1998, **176**, 113–133.
12 J. L. Vennerstrom, *J. Med. Chem.*, 1989, **32**, 64–67.
13 R. Gleiter, K. Hövermann, J. Ritter and B. Nuber, *Angew. Chem., Int. Ed.*, 1995, **34**, 789–791.
14 J. Kobayashi, K. Goto, T. Kawashima, M. W. Schmidt and S. Nagase, *J. Am. Chem. Soc.*, 2002, **124**, 3703–3712.
15 S. Nakafuji, J. Kobayashi, T. Kawashima and M. W. Schmidt, *Inorg. Chem.*, 2005, **44**, 6500–6502.
16 J. Kobayashi, K. Goto, T. Kawashima, M. W. Schmidt and S. Nagase, *Chem.–Eur. J.*, 2006, **12**, 3811–3820.
17 J. Kobayashi and T. Kawashima, *C. R. Chim.*, 2010, **13**, 1249–1259.
18 J. Tang, J. Dopke and J. G. Verkade, *J. Am. Chem. Soc.*, 1993, **115**, 5015–5020.
19 P. B. Kisanga, J. G. Verkade and R. Schwesinger, *J. Org. Chem.*, 2000, **65**, 5431–5432.
20 J. G. Verkade, *New Aspects in Phosphorus Chemistry II*, ed. J. P. Majoral, Springer, Berlin, Heidelberg, 2003, pp. 1–44.
21 M.-Y. Xu, W.-T. Jiang, Y. Li, Q.-H. Xu, Q.-L. Zhou, S. Yang and B. Xiao, *J. Am. Chem. Soc.*, 2019, **141**, 7582–7588.
22 D. Tanaka, A. Konishi and M. Yasuda, *Chem.–Asian J.*, 2021, **16**, 3118–3123.
23 M.-Y. Xu and B. Xiao, *Chem. Commun.*, 2021, **57**, 11764–11775.
24 J. K. Puri, R. Singh and V. K. Chahal, *Chem. Soc. Rev.*, 2011, **40**, 1791–1840.
25 S. N. Adamovich, *Appl. Organomet. Chem.*, 2019, **33**, e4940.
26 V. V. Istratov, V. A. Vasnev and G. D. Markova, *Molecules*, 2021, **26**, 1893.
27 S. N. Adamovich, I. A. Ushakov, E. N. Oborina, S. V. Lukyanova and V. Y. Komarov, *Int. J. Mol. Sci.*, 2023, **24**, 9965.
28 R. W. Alder, R. B. Sessions, J. M. Mellor and M. F. Rawlins, *J. Chem. Soc., Chem. Commun.*, 1977, 747–748.
29 R. W. Alder and R. B. Sessions, *J. Am. Chem. Soc.*, 1979, **101**, 3651–3652.
30 R. W. Alder, D. D. Ellis, R. Gleiter, C. J. Harris, H. Lange, A. G. Orpen, D. Read and P. N. Taylor, *J. Chem. Soc., Perkin Trans.*, 1998, **1**, 1657–1668.
31 R. W. Alder, C. P. Butts, A. G. Orpen and D. Read, *J. Chem. Soc., Perkin Trans.*, 2001, **2**, 288–295.
32 R. W. Alder, A. Casson and R. B. Sessions, *J. Am. Chem. Soc.*, 1979, **101**, 3652–3653.
33 R. W. Alder, R. J. Arrowsmith, A. Casson, R. B. Sessions, E. Heilbronner, B. Kovac, H. Huber and M. Taagepera, *J. Am. Chem. Soc.*, 1981, **103**, 6137–6142.
34 R. W. Alder, R. E. Moss and R. B. Sessions, *J. Chem. Soc. Chem. Commun.*, 1983, 997–998.
35 R. W. Alder, A. G. Orpen and R. B. Sessions, *J. Chem. Soc. Chem. Commun.*, 1983, 999–1000.
36 R. W. Alder, R. E. Moss and R. B. Sessions, *J. Chem. Soc. Chem. Commun.*, 1983, 1000–1002.
37 S. A. Harry, S. Vemulapalli, T. Dudding and T. Lectka, *J. Org. Chem.*, 2022, **87**, 8413–8419.
38 Y. Wang and Z.-X. Yu, *J. Org. Chem.*, 2020, **85**, 397–402.
39 Cage compounds with compressed CX–π interactions, called "iron maiden," were also studied.[64,65]
40 A. Karim, M. Reitti, A.-C. C. Carlsson, J. Gräfenstein and M. Erdélyi, *Chem. Sci.*, 2014, **5**, 3226–3233.
41 M. Bedin, A. Karim, M. Reitti, A.-C. C. Carlsson, F. Topić, M. Cetina, F. Pan, V. Havel, F. Al-Ameri, V. Sindelar, K. Rissanen, J. Gräfenstein and M. Erdélyi, *Chem. Sci.*, 2015, **6**, 3746–3756.
42 S. Lindblad, K. Mehmeti, A. X. Veiga, B. Nekoueishahraki, J. Gräfenstein and M. Erdélyi, *J. Am. Chem. Soc.*, 2018, **140**, 13503–13513.
43 L. Turunen and M. Erdélyi, *Chem. Soc. Rev.*, 2020, **49**, 2688–2700.
44 A. C. Reiersølmoen, S. Battaglia, S. Øien-Ødegaard, A. K. Gupta, A. Fiksdahl, R. Lindh and M. Erdélyi, *Chem. Sci.*, 2020, **11**, 7979–7990.
45 *Atoms in Molecules. A Quantum Theory*, ed. R. F. W. Bader, Oxford University Press, Oxford, UK, 1990.
46 C. F. Matta and R. J. Boyd, An Introduction to the Quantum Theory of Atoms in Molecules, in *The Quantum Theory of Atoms in Molecules: from Solid State to DNA and Drug Design*, ed. C. F. Matta and R. J. Boyd, WILEY-VCH, Weinheim, Germany, 2007, ch. 1.
47 W. Nakanishi and S. Hayashi, *Int. J. Quantum Chem.*, 2018, **118**, e25590.
48 K. Brandhorst and J. Grunenberg, *Chem. Soc. Rev.*, 2008, **37**, 1558–1567.
49 K. Brandhorst and J. Grunenberg, *J. Chem. Phys.*, 2010, **132**, 184101–184107.
50 M. J. Frisch, G. W. Trucks, H. B. Schlegel, G. E. Scuseria, M. A. Robb, J. R. Cheeseman, G. Scalmani, V. Barone, B. Mennucci, G. A. Petersson, H. Nakatsuji, M. Caricato, X. Li, H. P. Hratchian, A. F. Izmaylov, J. Bloino, G. Zheng, J. L. Sonnenberg, M. Hada, M. Ehara, K. Toyota, R. Fukuda, J. Hasegawa, M. Ishida, T. Nakajima, Y. Honda, O. Kitao, H. Nakai, T. Vreven, J. A. Montgomery Jr., J. E. Peralta, F. Ogliaro, M. Bearpark, J. J. Heyd, E. Brothers, K. N. Kudin, V. N. Staroverov, R. Kobayashi, J. Normand, K. Raghavachari, A. Rendell, J. C. Burant, S. S. Iyengar, J. Tomasi, M. Cossi, N. Rega, J. M. Millam, M. Klene, J. E. Knox, J. B. Cross, V. Bakken, C. Adamo, J. Jaramillo, R. Gomperts, R. E. Stratmann, O. Yazyev, A. J. Austin, R. Cammi, C. Pomelli, J. W. Ochterski, R. L. Martin, K. Morokuma, V. G. Zakrzewski, G. A. Voth, P. Salvador, J. J. Dannenberg, S. Dapprich, A. D. Daniels,

Ö. Farkas, J. B. Foresman, J. V. Ortiz, J. Cioslowski and D. J. Fox, *Gaussian 09, Revision D.01 and E.01*, Gaussian, Inc., Wallingford CT, 2009.

51 T. Noro, M. Sekiya and T. Koga, *Theor. Chem. Acc.*, 2012, **131**, 1–8.

52 C. Møller and M. S. Plesset, *Phys. Rev.*, 1934, **46**, 618–622.

53 E. D. Glendening, C. R. Landis and F. Weinhold, *J. Comput. Chem.*, 2013, **34**, 1429–1437.

54 F. Biegler-König, *J. Comput. Chem.*, 2000, **21**, 1040–1048.

55 T. A. Keith, *AIMAll (Version 17.11.14)*, TK Gristmill Software, Overland Park, KS, 2017, https://aim.tkgristmill.com/.

56 R. W. Alder and S. P. East, *Chem. Rev.*, 1996, **96**, 2097–2112.

57 The postulated symmetry was often broken during the optimizations, but not significantly altered.

58 P. Pyykkö and M. Atsumi, *Chem.–Eur. J.*, 2009, **15**, 186–197.

59 A. Bondi, *J. Phys. Chem.*, 1964, **68**, 441–451.

60 M. Mantina, A. C. Chamberlin, R. Valero, C. J. Cramer and D. G. Truhlar, *J. Phys. Chem. A*, 2009, **113**, 5806–5812.

61 W. Nakanishi, S. Hayashi, R. Imanaka, T. Nishide, E. Tanaka and H. Matsuoka, *Int. J. Mol. Sci.*, 2023, **24**, 2798.

62 D. B. DuPré, *J. Phys. Chem. A*, 2003, **107**, 10142–10148.

63 D. Cremer and E. Kraka, *Croat. Chem. Acta*, 1984, **57**, 1259–1281.

64 R. A. Pascal, *Eur. J. Org Chem.*, 2004, 3763–3771.

65 M. Jabłoński, *J. Comput. Chem.*, 2022, **43**, 1206–1220.